UPC **CTTC**

Joaquim Rigola Serrano

Numerical Simulation and Experimental Validation of Hermetic Reciprocating Compressors. Integration in Vapour Compression Refrigerating Systems.

DOCTORAL THESIS

Centre Tecnològic de Transferència de Calor
Departament de Màquines i Motors Tèrmics
Universitat Politècnica de Catalunya

Joaquim Rigola Serrano
Doctoral Thesis

UPC – September 2002

Numerical Simulation and Experimental Validation of Hermetic Reciprocating Compressors. Integration in Vapour Compression Refrigerating Systems.

Joaquim Rigola Serrano

TESI DOCTORAL

presentada al

Departament de Màquines i Motors Tèrmics
E.T.S.E.I.T.
Universitat Politècnica de Catalunya

per a l'obtenció del grau de

Doctor Enginyer Industrial

Terrassa, September 2002

Numerical Simulation and Experimental Validation of Hermetic Reciprocating Compressors. Integration in Vapour Compression Refrigerating Systems.

Joaquim Rigola Serrano

Directors de la Tesi

Dr. Carlos-David Pérez-Segarra

Dr. Assensi Oliva Llena

Tribunal Qualificador

Dr. Valeriano Ruiz Hernández
Universidad de Sevilla

Dr. Miquel Costa Pérez
Universitat Politècnica de Catalunya

Dr. Ramon Carreras Planells
Universitat Politècnica de Catalunya

Dr. Eduard Egusquiza Estévez
Universitat Politècnica de Catalunya

Dr. Antonio Lecuona Neumann
Universidad Carlos III de Madrid

Contents

Abstract

A detailed numerical simulation of the thermal and fluid dynamic behaviour of hermetic reciprocating compressors has been developed. The numerical simulation model presented is based on the integration of the fluid conservation equations (continuity, momentum and energy) in a transient and one-dimensional form along the whole compressor domain (compression chamber, valves, manifolds, mufflers, connecting tubes, parallel paths, etc.). Effective flow areas are evaluated considering multidimensional models based on modal analysis of fluid interaction in the valve. The force balances in the crankshaft connecting rod mechanical system are simultaneously solved at each time-step. The thermal analysis of the solid elements is based on global energy balances at each macro volume considered (shell, muffler, tubes, cylinder head, crankcase, motor, etc.).

The quality of the numerical solutions has been assessed by means of a critical analysis of the different numerical sources of errors: convergence errors, discretization errors and programming errors. The results make clear the influence of the different numerical parameters: time-step, transient order schemes, number of grid nodes, etc.

An extensive experimental validation of the numerical simulation model has been carried out. Global experimental tests have been performed both in a standard calorimeter set-up and in a laboratory set-up for different refrigerant fluids, compressor capacities and working conditions. Furthermore, two commercial hermetic reciprocating compressors have been instrumented in detail to obtain the thermal temperatures map and the pressure fluid evolutions along the compressor domain, considering different working conditions. The accuracy of the mathematical model developed (modelling errors) has been verified by means of these comprehensive experimental studies.

A review of different hermetic reciprocating compressors parameters performances has been carried out (volumetric efficiency, isentropic efficiency, heat transfer efficiency, mechanical, electrical and heat losses, coefficient of performance, etc.). The parameters selection, a novel detachment of some of them and their physical meaning have been presented. Different illustrative numerical cases have been also presented in order to show the importance of these parameters in compressor behaviour and how parameters detachment can help to improve compressor performance.

Finally, a wide range of parametric studies have been developed considering: geometrical aspects (valves shapes, orifices, mufflers, resonators, etc.), boundary conditions, working fluids, electrical motors, etc. These studies show the capabilities of the mathematical and numerical model developed and point out the different aspects which limit the performance of these compressors.

Acknowledgements

A l'Assensi, alma mater del Laboratori, per la seva capacitat d'encoratjar, entusiasmar i fer-te participar a tu i a tothom en tot allò que fem. Va ser el primer professor que em va motivar de forma molt especial amb l'assignatura de Calor i Fred i amb totes les temàtiques que hi havia al darrera. I perquè tot el que vas aprenent amb ell va molt més enllà dels indiscutibles aspectes professionals.

Al David, per la dedicació i lliurament amb que treballa, t'ensenya i ajuda en tot el que fa falta. I perquè és un tutor d'una rigorositat i professionalitat indiscutibles. Algun dia la Universitat haurà de fer-li justícia.

I perquè és un luxe haver-los tingut com a directors de Tesi.

Al Miquel que sempre s'interessa per qualsevol dubte que puguis tenir, i te un moment per tu. I perquè els ensurts que de vegades dóna la vida quedin només amb això.

Al Jordi i al Ricard per tot el que hem viscut, ens hem divertit i hem disfrutat junts durant aquests anys, i sens dubte per l'amistat que tenim.

Al Ramiro que sempre el pots localitzar allà on estigui per solucionar qualsevol problema amb els ordinadors, encara que estigui de vacances a Galícia o a Astúries.

Al Gustavo per tota la feina que ha realitzat a la part experimental de pV i l'interès incansable de profunditzar més en tot. Per la motivació amb que treballa i amb què ho transmet.

Al Manolo per tot el suport i ajuda en els muntatges experimentals i les moltes ganes de fer-ho bé. Sempre mira a veure si allò ho podem muntar d'una manera millor.

Al Manel que amb el seu contrapunt en el treball i en les classes, dona una visió diferent i enriquidora de les coses. Perquè tot allò que diu sempre et fa pensar.

Al Josep Maria Serra, Josep Pons, Manel Escribà, Jaume Jornet, Alfons Castillo, Joaquim Jover, Ferran Escanes i Toni Chacón de l'empresa Unidad Hermética per l'interès, les ganes en el treball conjunt amb el Laboratori i l'ajuda tècnica i material en els diferents projectes de col.laboració.

A tots el companys del Laboratori i a totes aquelles persones que d'una manera o una altre han fet possible aquest treball.

A l'Associació d'Enginyers Industrials de Catalunya per la beca de realització de la Tesi Doctoral 1999, amb el suport de Caixa d'Enginyers.

Al Ministeri d'Educació i Ciència per la beca d'estudiant de doctorat.

A la Lidia
Als meus pares

Chapter 1

Introduction

1.1 Preamble

The first compression machines for refrigeration were developed during 1860-1875. One of the basic elements of a vapour compression refrigerating system is the compressor. Little changes took place from the end of XIX century to the beginning of the XX century. Between 40s to 60s compressors were improved basically by increasing compressor speed and improving valve design. At the beginning of the 1970s, the energy crisis obliges to improve efficiencies. In 1987 the Montreal Protocol [1] appears with the idea to protect the stratospheric ozone layer and stipulates to phase out chlorofluorocarbons (CFCs) and hydrochlorofluorocarbons (HCFCs) refrigerants like compounds that deplete ozone layer. Then, the group of useful refrigerants was reduced to hydrofluorocarbons (HFCs) and natural refrigerants. In 1997 the Kyoto Protocol [2] determinates "to achieve stabilization of atmospheric concentrations of greenhouse gases at levels that would prevent dangerous anthropogenic (human-induced) interference with the climate system..." and encourages to promote policies and measures to sustainable development. The global warming potential (GWP) of HFC gases is high, which obliges that these kind of gases have to be regulated. Thus, the necessity to develop and optimise more efficiency compressors became particularly important.

Different compressor types are used in the refrigeration field [3][4]: dynamics (centrifugal, axial, radial, etc.) and positive displacement (rotary, screw, scroll, reciprocating, etc.). Positive displacement compressors mechanically drive the refrigerant gas from the evaporator at low-pressure side, to the condenser at high-pressure side, reducing the compression chamber volume. Reciprocating compressors use pistons that are driven directly through a pin and connecting rod from the crankshaft. Hermetic reciprocating compressors are a particular case where motor and crankshaft are contained within the same housing and in contact with the refrigerant and oil.

Figs. 1.1 and 1.2 show a schematic and general representation of a commercial

hermetic reciprocating compressor which is representative of all compressors numerically and experimentally tested in this Thesis. The way these compressors works is as follows. The low-pressure dry gas from the evaporator enters the space situated between the shell and the motor-compressor unit, i.e. crankcase and electrical motor. After that, it goes across the suction ducts to the cylinder, where the piston compresses the gas raising its pressure. Finally, the high-pressure gas is discharged from the cylinder to discharge plenum and goes through the impulsion ducts to the condenser. The gas on its way across the suction and discharge ducts goes through different elements such as tubes, mufflers, manifolds, valves, compression chamber, etc.

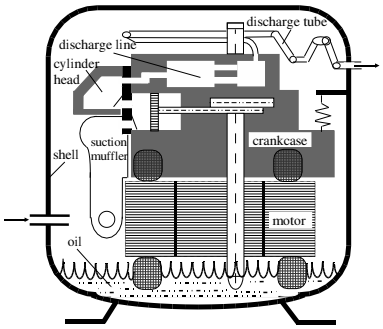

Figure 1.1: Compressor scheme.

Figure 1.2: General compressor view.

Most cooling systems in use today rely on reciprocating piston type compressors. Hermetic reciprocating compressors are typically used in household refrigerators and freezers, residential air conditioners, small commercial air conditioning for low capacity and commercial refrigerating units like: food services, ice machines, beverage dispenser or condensing units.

Single stage vapour compression cycle is the most important commercial refrigerating cycle for refrigerators, small capacity refrigeration units and residential air source heat pumps. Real vapour compression cycle has to take into account: i) heat transfer with finite temperature differences and pressure drop through the different heat exchangers, ii) sub-cooling liquid and super-heating vapour inside condenser and evaporator respectively, iii) heat exchanged through expansion system and iv) non-isentropic and non-adiabatic real compressor behaviour. Other systems can be required for other refrigeration applications: cascade cycles, i.e. two or more refrigerating systems, where one is acting as condenser to the other; liquid overfeed systems which includes a low pressure receiver; etc.

1.2 Literature review

Thermal and fluid dynamic behaviour of hermetic reciprocating compressors are characterized by complex heat transfer and fluid flow phenomena: three-dimensional, turbulent, compressible flow, fast transient and pulsatory processes, complex geometries, moving surfaces, etc. The challenge of new refrigerants and the need for high efficiencies are strong incentives to develop general and accurate prediction methodologies.

Different compressor simulation models are present in the technical literature. Three groups are here considered.

A first group of models evaluates thermodynamically the behaviour of hermetic reciprocating compressors at periodical conditions, i.e., cyclical or quasi steady state conditions, by means of global energy and mass balances including spring-mass valve dynamic models. Soedel [5] takes into account pressure pulsation effects. Prakash et al. [6] add second law analysis and irreversibilities losses, while Singh [7] compares experimentally valve displacements, pressure pulsations and pV diagram.

A second group of models presents a more advanced simulation strategies based on the whole conservation laws: continuity, momentum and energy. MacClaren et al. [8] solve hyperbolic partial differential equations for unsteady one-dimensional compressible fluid flow by the method of characteristics. Morel et al. [9] develop a numerical model to solve the quasi-one dimensional compressible flow conservation equations applying finite-volume approach. The time-differencing is based on the explicit technique and a staggered mesh is used to evaluate the momentum equation. Heat transfer and friction losses terms are evaluated as source terms. Pérez-Segarra et al. [10] and Escanes et al. [11] develop a detailed numerical simulation of the one-dimensional and transient governing equations of the flow in the whole domain by means of a fully implicit control volume formulation using a pressure-based method.

Both the first and the second group of models need some closure relations, such as pressure drop coefficients across tubes and singularities (valves, orifices, sudden expansions and contractions) or convection heat transfer (see details and references in paragraph 2.8).

The third group of models, which constitutes the highest level of simulation, are based on the numerical solution of the governing equations of the flow in multidimensional and transient form. The simulation allows the detailed determination of the local velocity, pressure, density and temperature distributions in the whole domain without the need of empirical information (except for the empirical constants and functions when turbulence models are employed). Although the computational time required is prohibitively large for design purposes, and turbulence models introduce uncertainties, these methodologies can give very valuable information. For example, different numerical studies of the multidimensional flow behaviour in the compression chamber have been carried out to obtain local heat transfer coefficients (Recktenwald [12], Polman [13] and Kornhauser et al. [14]). Other numerical studies

have been focused on evaluating multidimensional flow through valves (Cyklis [15], Deschamps et al. [16] and Pérez-Segarra et al. [17]). Finally, several numerical simulations solve multidimensional heat transfer phenomena in sudden expansions under pulsating conditions for suction and discharge chambers (Ma et al. [18], Ibrahim et al. [19] and Mladin et al. [20]). Although the computational time required is prohibitively large for design purposes and turbulence models introduce uncertainties, these methodologies can give very valuable information.

Concerning to numerical simulation models of the thermal and fluid dynamic behaviour of single stage vapour compression systems, and specially focused on numerical integration of the different components and modelization of the overall systems, several models presented in the technical literature, focusing their attention on simulating typical vapour compression systems, their components, the overall refrigeration cycle and their experimental comparison.

Among them, the models developed by Chi and Didion [21], Murphy and Goldsmith [22][23] and Rajendran and Pate [24] are based on global balances between the inlet and outlet sections of the different elements of the system. MacArthur [25], Jung and Radermacher [26] and Yuan and O'Neal [27][28] solve the condenser and the evaporator using finite difference methods and considering a one dimensional formulation of the governing equations. There is no comparison with experimental data. MacArthur [25] solves the compressor and the expansion valve using parametric models based on non-dimensional correlations. Jung and Radermacher [26] work with pure and mixed refrigerants considering a non-ideal isentropic compressor and solving the simulation system using two possible methods: the successive substitution and the Newton-Raphson method. Yuan and O'Neal [27][28] consider the compressor as a polytropic process, and the suction and discharge valves adiabatic and isenthalpic, while the pressure drop in the condenser and evaporator is not considered. Escanes et al. [29] present a complete simulation of the whole compressor system. The model is based on a segregated resolution of the different elements of the system considering steady and unsteady situations and a detailed modelization of most of the components (heat exchangers, expansion devices, connecting tubes).

1.3 Objectives

This Thesis represents a step forward in the activities of the CTTC (Centre Tecnologic de Transferencia de Calor) in the refrigeration field. This activity began in 1990 within a close collaboration with the company Unidad Hermetica, S.A. (nowadays CUBIGEL,S.A. of Electrolux Compressors). This collaboration has been maintained and consolidated during all these years. Initially, attention was focussed on the rigorous analysis of the components (condensers, evaporators, expansion devices) and their coupling on the whole refrigerating cycle [29]. When this Thesis began, a first

detailed simulation model of the compressor had already been developed [30]. However, more effort was needed to develop a more general simulation code for hermetic reciprocating compressors. Within this perspective, the objectives of this Thesis have been: i) to contribute in the development of an advanced and detailed numerical simulation model of the thermal and fluid dynamic behaviour of hermetic reciprocating compressors, specifically: complex internal circuitry, valve dynamics, heat transfer in solid elements, mechanical transmission and electrical motor, etc. ii) to build an experimental infrastructure to study in detail the compressor behaviour under a wide range of operating conditions (detail temperature distribution, pV diagram, etc.); iii) to compare numerical and experimental results in order to validate the mathematical models; iv) to review and create a new parameters to characterize global behaviour of these compressors (volumetric efficiency, isentropic efficiency, heat transfer efficiency, mechanical and electrical motor efficiency, coefficient of performance, COP, etc.) based on the possibilities of the numerical model developed; v) to analyze the influence of different aspects (geometry, boundary conditions, refrigerant fluids, etc.) which limits the performance of these compressors, helping to obtain optimum design.

References

[1] (UNEP). United Nations Environmental Programme. Montreal Protocol on substances that deplete the ozone layer, 1987.

[2] (UNFCCC). United Nations framework convention on climate change. Kyoto Protocol, 1997.

[3] ASHRAE Handbook. *HVAC Systems and Equipment*. 2000. pp. 34.1–34.36.

[4] W.F. Stoecker and J.W. Jones. *Refrigeration and Air-Conditioning*. Mc-Graw Hill, 2nd ed, N.Y., USA, 1982. pp. 34.1–34.36.

[5] W. Soedel. *Introduction to computer simulation displacement type compressors*. Purdue University Short Courses, IN, USA, 1972.

[6] R. Prakash and R. Singh. Mathematical modeling and simulation of refrigerating compressors. In *International Compressor Engineering Conference*, pages 274–285, Purdue University, IN, USA, 1974.

[7] P. J. Singh. A digital reciprocating compressor simulation program including suction and discharge piping. In *International Compressor Engineering Conference*, pages 129–138, Purdue University, IN, USA, 1984.

[8] J.F.T. MacClaren, A.B. Tramscheck, A. Sanjines, and D.F. Pastrana. A comparison of numerical solutions of the unsteady flow equations applied to reciprocating compressor systems. *Journal Mechanical Engineering Science*, 17(5):271–279, 1975.

[9] T. Morel and R. Keribar. Comprehensive model of a reciprocating compressor applicable to component design issues. In *International Compressor Engineering Conference*, pages 375–384, Purdue University, IN, USA, 1988.

[10] C.D. Pérez-Segarra, F. Escanes, and A. Oliva. Numerical study of the thermal and fluid dynamic behaviour of reciprocating compressors. In *International Compressor Engineering Conference*, pages 145–150, Purdue University, IN, USA, 1994.

[11] F. Escanes, C.D. Pérez-Segarra, J. Rigola, J.M. Serra, J. Pons, M. Escribà, and M. Jornet. Numerical simulation of reciprocating compressors. recent improvements and experimental validation. In *International Compressor Engineering Conference*, pages 193–198, Purdue University, IN, USA, 1996.

[12] G.W. Recktenwald. *Numerical modelling of the flow and Heat Transfer in the Cylinder of a Reciprocating Compressor*. PhD thesis, Purdue University, Indiana, USA, 1986.

[13] J. Polman. Heat transfer in a piston-cylinder system. *International Journal of Heat and Mass Transfer*, 24(shorter communications):184–187, 1981.

[14] A.A. Kornhauser and Jr. Smith, J.L. Application of a complex nusselt number to heat transfer during compression and expansion. *Journal of Heat Transfer*, 116:536–542, 1994.

[15] P. Cyklis. Cfd simulation of the flow through reciprocating compressor self-acting valves. In *International Compressor Engineering Conference*, pages 427–432, Purdue University, IN, USA, 1994.

[16] C.J. Deschamps, R.T.S. Ferreira, and A.T. Prata. Turbulent flow through valves of reciprocating compressors. In *International Compressor Engineering Conference*, pages 377–381, Purdue University, IN, USA, 1996.

[17] Pérez-Segarra, J. C.D., Cadafalch, J. Rigola, and A. Oliva. Numerical study of turbulent fluid flow through valves. In *International Conference on Compressors and Their Systems*, pages 399–408, City University, London, UK, 1999.

[18] P. Ma, X. Li, and D.N. Ku. Heat and mass transfer in a separated flow region for high prandtl and schmidt numbers under pulsatile conditions. *International Journal of Heat and Mass Transfer*, 37(17):2723–2836, 1994.

[19] M. Ibrahim and W. Hashim. Oscillating flow in channels with a sudden change in cross section. *Computer Fluids*, 23(1):211–224, 1994.

[20] E.C. Mladin and D.A. Zumbrunnen. Dependence on heat transfer to a pulsating stagnation flow on pulse characteristics. *Journal of Thermophysics and Heat Transfer*, 9(1):181–192, 1995.

[21] J. Chi and D. Didion. A simulation model of the transient performance of a heat pump. *International Journal of Refrigeration*, 5(3):176–184, 1982.

[22] W.E. Murphy and V.W. Goldschmidt. Cyclic characteristics of a typical residential air conditioner-modeling of start-up transients. *ASHRAE Transactions*, 91(2):427–444, 1985.

[23] W.E. Murphy and V.W. Goldschmidt. Cyclic characteristics of a residential air conditioner-modeling of shutdown transients. *ASHRAE Transactions*, 92(1):186–202, 1986.

[24] N. Rajendran and M.B. Pate. A computer model of the start-up transients in a vapor compression refrigeration system. In *Progress in the Design and Construction of Refrigeration Systems*, pages 129–140, Purdue University, IN, USA, 1986. International Institute of Refrigeration.

[25] J.W. MacArthur. Transient heat pump behaviour: a theoretical investigation. *International Journal of Refrigeration*, 7(2):123–132, 1984.

[26] D.S. Jung and R. Radermacher. Performance simulation of a two-evaporator refrigerator-freezer charged with pure and mixed refrigerants. *International Journal of Refrigeration*, 14:254–263, 1991.

[27] X. Yuan and D.L. O'Neal. Development of a transient simulation model of a freezer parti: Model development. In *International Refrigeration and Air Conditioning Conference*, pages 213–218, Purdue University, IN, USA, 1994.

[28] X. Yuan and D.L. O'Neal. Development of a transient simulation model of a freezer partii: Comparison of experimental data with model. In *International Refrigeration and Air Conditioning Conference*, pages 219–224, Purdue University, IN, USA, 1994.

[29] F. Escanes, A. Oliva, C.D. Pérez-Segarra, and F.X. Flores. Numerical simulation of a single stage vapour compression refrigerating unit. In *International Compressor Engineering Conference*, pages 139–144, Purdue University, IN, USA, 1994.

[30] F. Escanes. *Numerical simulation of the thermal behaviour of diferent components of compression refrigerating system. Experimental validation. Application to noncontaminant rerigerants.* PhD thesis, Technical University of Catalonia, UPC, CTTC, UPC, Terrassa, Barcelona, 1995.

Chapter 2

Mathematical formulation and numerical aspects

2.1 Introduction

A detailed numerical simulation of the thermal and fluid dynamic behaviour of reciprocating compressors commonly used in household refrigerators and freezers has been developed. The model is based on the integration of the transient fluid conservation equations (continuity, momentum and energy) in the whole compressor domain (compression chamber, valves, manifolds, mufflers, connecting tubes, parallel paths, etc.) using instantaneous local mean values for the different variables. Effective flow areas are evaluated considering multidimensional models based on modal analysis of fluid interaction in the valve. In order to evaluate the instantaneous compression chamber volume, force balances in the crankshaft connecting rod mechanical system are simultaneously solved at each time-step. The thermal analysis of the solid elements is based on global energy balances at each macro volume considered (shell, muffler, tubes, cylinder head, crankcase, motor, etc.). The resulting governing equations (fluid flow, valve dynamics, conduction heat transfer in solids, etc.) are discretized by means of a fully implicit control volume formulation. The complete set of algebraic equations are coupled using the segregated pressure based algorithm Semi-Implicit Method for Pressure-Linked Equations (SIMPLEC) extended to compressible flow. A detailed numerical analysis is presented with the aim to verify the quality of the numerical solution.

2.2 Governing equations and numerical model

The basic governing equations describe the principles of conservation of space, mass, linear momentum and energy. In an arbitrary spatial region of volume $V(t)$, bounded

by a closed surface $S(t)$ in the Euclidean space, which is moving with a velocity $\vec{v}_b$, the above mentioned conservation principles can be written in the form [1]:

$$\frac{d}{dt}\int\limits_V dV - \int\limits_S \vec{v}_b \cdot \vec{n} dS = 0 \tag{2.1}$$

$$\frac{d}{dt}\int\limits_V \rho dV + \int\limits_S \rho(\vec{v} - \vec{v}_b) \cdot \vec{n} dS = 0 \tag{2.2}$$

$$\frac{d}{dt}\int\limits_V \vec{v}\rho dV + \int\limits_S \vec{v}\rho\,(\vec{v} - \vec{v}_b) \cdot \vec{n} dS = \int\limits_S \vec{n} \cdot \vec{\sigma} dS + \int\limits_V \vec{b}\rho dV \tag{2.3}$$

$$\begin{gathered}\frac{d}{dt}\int\limits_V (u + e_c)\,\rho dV + \int\limits_S (u + e_c)\,\rho\,(\vec{v} - \vec{v}_b) \cdot \vec{n} dS = \\ -\int\limits_S \vec{q} \cdot \vec{n} dS + \int\limits_S \vec{v} \cdot (\vec{n} \cdot \vec{\sigma})\,dS + \int\limits_V \vec{v} \cdot \vec{b}\rho dV + \int\limits_V \Phi\rho dV\end{gathered} \tag{2.4}$$

In these equations $\vec{n}$ represents the outward unit vector of the surface S. It should be noticed that external forces are represented by the stress tensor σ which includes pressure forces and shear stresses.

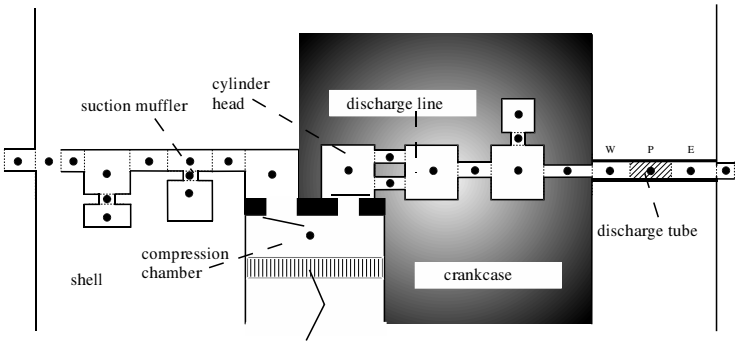

Figure 2.1: General compressor flow domain. Control volumes and grid nodes.

The numerical model is based on the division of the whole compressor domain (tubes and chambers where the gas is flowing, shell, crankcase, oil, etc.) into strategically distributed control volumes (CVs). Fig. 2.1 shows a schematic representation of both control volume and grid node distribution along the gas flow domain.

Some parts of the compressor, such as the gas in the mufflers or in the compression chamber, constitute single CVs and they cannot be divided into smaller ones. Other parts, such as the gas in the tubes or the different solid elements, can be divided into an arbitrary number of CVs. For each CV a grid node is assigned at its center. In Fig. 2.1 example, suction muffler is divided into 8 CVs, discharge line is composed by 8 CVs, while discharge tube is divided into 3 CVs.

For the fluid flow, pressure, temperature and density are calculated from continuity equation (2.2), energy equation (2.4) and state equation $f(\rho, p, T) = 0$ respectively. These variables are evaluated at each grid node of the control volumes which contains the refrigerant pulsating gas considered (Fig. 2.2a). The compression chamber volume is changing along the time and the space conservation equation (2.1) is needed. Velocities are determined from the momentum equation (2.3) at the faces of the main control volumes using staggered volumes (Fig. 2.2b).

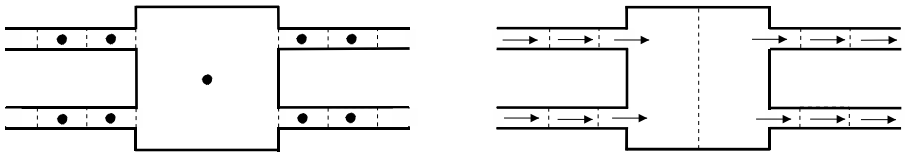

Figure 2.2: (a) left: main control volumes. (b) right: staggered control volumes.

This procedure not only avoids decoupling between continuity and momentum equations, but is also an excellent way to handle the abrupt cross section changes characteristic of this type of geometries. For the solid elements only the energy equation is needed. A simple form results from equation (2.4). Other important aspect such as valve dynamics only involves momentum equation. In the next subsections the discretized equations of the different volumes, together with the necessary empirical inputs, are going to be presented in detail.

2.3 Discretized governing equations for the gas flow

For whatever of the CVs in which the refrigerant gas is flowing (see Fig. 2.1), the general governing equations (2.1) to (2.4) can be written, in terms of the local averaged fluid variables, neglecting body forces and both axial shear stresses and axial heat conduction, in the following form:

$$\frac{\partial m}{\partial t} + \sum \dot{m}_o - \sum \dot{m}_i = 0 \tag{2.5}$$

$$\frac{\partial m\bar{v}}{\partial t} + \sum \dot{m}_o v_o - \sum \dot{m}_i v_i = F_s \tag{2.6}$$

$$\frac{\partial m\left(\bar{h} + \bar{e}_c\right)}{\partial t} + \sum \dot{m}_o \left(h_o + e_{co}\right) - \sum \dot{m}_i \left(h_i + e_{ci}\right) = V\frac{\partial \tilde{p}}{\partial t} + \dot{Q}_w \tag{2.7}$$

The instantaneous mass contained in the CV is evaluated as $m = \int_V \rho dV$, while the mass flow rate at a given cross-section S_k is calculated as $\dot{m}_k = \int_{S_k} \rho\left(\vec{v} - \vec{v}_b\right) \cdot d\vec{S}$. The local averaged fluid variables at a given flow cross-section S_k are evaluated as $\phi_k = \frac{1}{\dot{m}_k} \int_{S_k} \rho\phi\left(\vec{v} - \vec{v}_b\right) \cdot d\vec{S}$, where ϕ represents a generic variable $(v, h, e_c, etc.)$.

Over-bars and tildes indicate integral mass and volume averages over the CV respectively, that is: $\bar{\phi} = \frac{1}{m} \int_V \phi\rho dV$ and $\tilde{\phi} = \frac{1}{V} \int_V \phi dV$. The energy equation has been written in terms of enthalpy h instead of the internal energy u. Furthermore, only the work performed by pressure forces has been considered. Note that $v = v_b = 0$ at the control volume faces in contact with the solid elements, except in the compression chamber where, at the piston base, both the fluid and the CV face velocities are equal to the piston velocity. From the space conservation law (1), the piston velocity and the volume changes in the compression chamber can be easily related.

2.3.1 Momentum equation

The momentum equation only involves one inlet and outlet flow stream sections because the equation is applied over staggered CVs (Fig. 2.2b). The surface force F_s in the flow direction acting on the surfaces of the CV depends on its geometry. Thus, for the CVs with uniform cross-sectional area S_s, the momentum equation (2.6) takes the form:

$$\frac{\partial m\bar{v}}{\partial t} + \dot{m}_o v_o - \dot{m}_i v_i = \left(p_i - p_o\right) S_s - \frac{f}{4}\frac{|\dot{m}|\,\bar{v}}{2S_s} P\Delta z \tag{2.8}$$

When a singularity is presented, such as a sudden enlargement or a sudden contraction (Fig. 2.3), the following equation is obtained from a momentum balance.

$$l\frac{\partial \dot{m}}{\partial t} + \frac{|\dot{m}|\,v_s}{2}\left[\left(\frac{1}{\sigma_o^2} - \frac{1}{\sigma_i^2}\right) + \left(\frac{1}{\sigma_o} - \frac{1}{C_c}\right)^2\right] = \left(p_i - p_o\right) S_s \tag{2.9}$$

Equation (2.9) has been obtained assuming: i) one-dimensional incompressible flow; ii) isentropic flow behaviour from the inlet section 'i' to the vena contracta 'c'; iii) the pressure on the back face of the orifice 's' is equal to the plenum pressure 'o'.

The cross-sectional area ratios σ and the contraction coefficient C_c are evaluated as $\sigma_i = S_i/S_s$, $\sigma_o = S_o/S_s$ and $C_c = S_c/S_s$. The length l in the unsteady term of the momentum equation is composed by the actual length of the constriction plus a correction term to allow for the extra fluid speeding up and slowing down at the two ends. This value has been estimated from the kinetic energy induced by the singularity assuming irrotational steady flow [2].

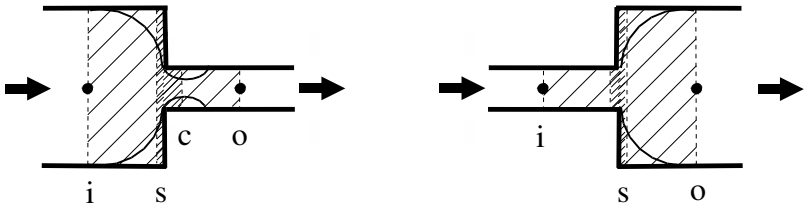

Figure 2.3: (a) left: sudden contraction. (b) right: sudden enlargement.

In general, the assumption of incompressible gas flow is reasonable in most parts of the compressor domain. When the Mach number is high (typically higher than 0.3) compressibility effects are significant. This is the case of the flow in the valve, where an equation derives in a similar way to equation (2.9), but extended to compressible flow, is used to evaluate the mass flow [3]. The resulting equation is:

$$l\frac{\partial \dot{m}}{\partial t} + \frac{|\dot{m}|\, v_s}{2} \cdot \frac{\gamma - 1}{\gamma} \cdot \frac{1 - p_o/p_i}{\Pi^{1/\gamma} - \Pi} = (p_i - p_o)\,(KS)_s \tag{2.10}$$

The parameter Π depends on the flow conditions. In supersonic flow conditions $\Pi = \Pi_c = (2/\gamma + 1)^{(\gamma/(\gamma-1))}$, while under subsonic flow conditions $\Pi = p_o/p_i > \Pi_c$. Then, $\Pi = max(p_o/p_i, \Pi_c)$ in both cases. The effective flow area through the valve orifice $(KS)_S$, depends on geometry valve and its instantaneous displacement. Effective flow area is evaluated by means of semi-analytical models [4] considering two serial restrictions: axial flux through orifice $(KS)_a$ plus radial flux through port area $(KS)_r$, i.e., $(KS)_s^{-2} = (KS)_a^{-2} + (KS)_r^{-2}$. For a valve system with several orifices, the effective flow area $(KS)_s$ is evaluated considering parallel restrictions.

2.3.2 Energy equation

The energy equation (2.7) is obtained in a more suitable way (2.11) if the equation resulting of multiplying the continuity equation (2.5) by the specific enthalpy h_P at the central node P of the CV at a given instant of time is added to the energy equation (2.7):

$$\begin{aligned}\frac{\partial m\left(\bar{h}-h_P\right)}{\partial t}+\sum_o \dot{m}\left(h-h_P\right)-\sum_i \dot{m}\left(h-h_P\right)= \\ V\frac{\partial \tilde{p}}{\partial t}-\left[\frac{\partial m\bar{e}_c}{\partial t}+\sum_o \dot{m}e_c-\sum_i \dot{m}e_c\right]+\dot{Q}_w\end{aligned} \tag{2.11}$$

Taking into account that the enthalpy of the super-heated gas is a function of both temperature and pressure, enthalpy differences are accurately evaluated by integrating:

$$dh = c_p dT + \frac{1-\beta T}{\rho}dp \tag{2.12}$$

The inlet heat flux through the solid boundaries is evaluated using the local heat transfer coefficient, $\dot{Q}_w = \int_{A_P} \alpha_P \left(T_{wall}-T_P\right) dA$, which is usually calculated at the central node conditions, i.e., $\dot{Q}_w \approx \alpha_P \left(\bar{T}_{wall}-T_P\right) A_P$.

2.3.3 Final discretization form of the gas flow equations

For each one of the CVs in which the domain is divided, the final form of the semi-discretized flow equations given above, continuity (2.5), momentum (2.8, 2.9 and 2.10) and energy (2.11), are obtained considering different aspects.

The equations are integrated in time using a fully implicit scheme, that is, all convective diffusion and source terms are evaluated at the actual time level indicated with the superscript n.

Unsteady terms are evaluated using a first or a second order backward differencing scheme, that is: $\partial\phi/\partial t \approx \left(\phi^n-\phi^{n-1}\right)/\Delta t$ or $\partial\phi/\partial t \approx \left(3\phi^n-4\phi^{n-1}+\phi^{n-2}\right)/2\Delta t$, where Δt denotes the selected time-step. The extension of the second order scheme to non-constant time-steps is straightforward.

Average values are numerically approximated using nodal values, that is, $\bar{\phi}\approx\phi_P$ or $\tilde{\phi}\approx\phi_P$. Using this approximation and, for example the first order scheme, the unsteady term in the energy equation (11) can be evaluated as $\partial m\left(\bar{h}-h_P^n\right)/\partial t \approx \rho_P^{n-1}V_P^{n-1}\left(h_P^n-h_P^{n-1}\right)/\Delta t$.

Convective terms at the CV faces, $\dot{m}_k \phi_k$, are evaluated using first or higher order convective schemes. When a first order scheme is used, the variables at a given face of the CV are taken equal to the nearest upstream nodal values (this is the well-known upwind differencing scheme).

Higher order schemes for the convective terms are introduced using a deferred correction approach (the convective term is evaluated using the first order upwind scheme plus a correction term which is introduced in the source term of the discretized equation keeping the diagonal dominance of the coefficient matrix). It is worth while to mention that the upstream influence of the convective transport variable is often broken by the presence of chambers.

Introducing the numerical criteria indicated above in the continuity equation, and considering the first order backward differencing scheme for the unsteady term, the following discretized equation is obtained:

$$\frac{\rho_P^n V_P^n - \rho_P^{n-1} V_P^{n-1}}{\Delta t} + \sum_o (\rho v S)^n - \sum_i (\rho v S)^n = 0 \tag{2.13}$$

For the momentum and energy equations the following generic form of the discretized equation is obtained at each CV:

$$a_P^\phi \phi_P^n = \sum a_{nb}^\phi \phi_{nb}^n + b_P^\phi \tag{2.14}$$

For example, the application of the energy equation to the CV indicated in the discharge line of Fig.2.1, gives the following discretization coefficients:

$$a_P^T = \frac{m_P^{n-1} c_{p,P}}{\Delta t} + max\left(\dot{m}_w, 0\right) c_{p,w} + max\left(-\dot{m}_e, 0\right) c_{p,e} + \alpha_P A_P \tag{2.15}$$

$$a_E^T = max\left(-\dot{m}_e, 0\right) c_{p,e} \tag{2.16}$$

$$a_W^T = max\left(\dot{m}_w, 0\right) c_{p,w} \tag{2.17}$$

$$\begin{aligned} b_P^T = {} & \frac{m_P^{n-1} c_{p,P}}{\Delta t} T_P^{n-1} - \frac{\left(1 - \beta_P T_P\right)}{\rho_P} \frac{\left(p_P^n - p_P^{n-1}\right)}{\Delta t} \\ & - max\left(\dot{m}_w, 0\right) \frac{\left(1 - \beta_w T_w\right)}{\rho_w} \left(p_P^n - p_W^n\right) - max\left(-\dot{m}_e, 0\right) \frac{\left(1 - T_e \beta_e\right)}{\rho_e} \left(p_P^n - p_E^n\right) \\ & + V_P \frac{\left(p_P^n - p_P^{n-1}\right)}{\Delta t} + \alpha_P A_P T_w \end{aligned} \tag{2.18}$$

The discretized set of governing equations are directly solved using the Tri-Diagonal Matrix Algorithm (TDMA). When the piping system includes parallel paths and/or leakage through the piston, the matrix of the discretized coefficients is not tri-diagonal. In this case, the set of the equations is iteratively solved using a line by line solver [5].

2.4 Effective valve flow area evaluation

Valve position and effective valve flow area are necessary to evaluate momentum equation (2.10) in fluid-solid interaction through valves. The simplest model to evaluate valve position is assuming a spring-loaded ring valve governed by a one degree of freedom valve motion. This model is based on a momentum balance, accounting for the drag, spring and damping forces acting at each instant on the reed valves. The resulting second-order differential equation has the form [6].

$$\ddot{w}(t) + 2\xi\omega_n\dot{w}(t) + \omega_n^2 w(t) = A_F \Delta p(t)/m_v \tag{2.19}$$

where $\ddot{w}$ is the instantaneous mean valve acceleration, $\dot{w}$ is the instantaneous mean valve velocity and w is the mean valve position. The damping coefficient ξ is defined as $\xi = C/2m_v\omega_n$ and the instantaneous force acting over the valve can be written in terms of effective force area, i.e., $F = A_F\Delta p(t)$.

For a more accurate description of the typical flexible reed valves used in these compressors (i.e., thin plate, short displacement and transverse deflection) a multidimensional model is needed. Force balance considered under the hypothesis mentioned below are shown in Fig. 2.4.

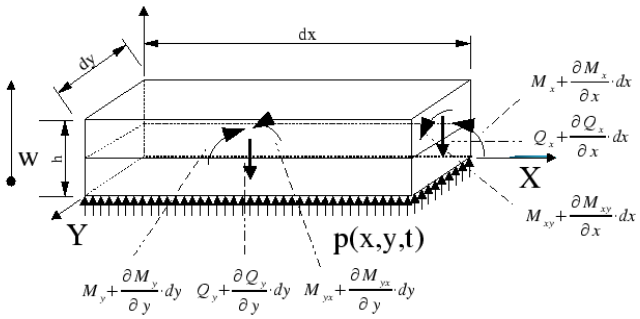

Figure 2.4: Free body forces under valve reed element.

The force balances through the free body considered as a plate element, with a neutral surface in the middle plane, without normal stress and without any movement in the point perpendicular to middle plane, the following equation of motion is obtained [6]:

$$D\nabla^4 w\left(x,y,t\right)+\rho h_v \ddot{w}\left(x,y,t\right)=p\left(x,y,t\right) \tag{2.20}$$

where the local valve velocity and acceleration are denoted by $\dot{w}\left(x,y,t\right)$ and $\ddot{w}\left(x,y,t\right)$, $p(x,y,t)$ denotes the local net force per unit area acting on the valve. and $D=Eh_v^3/12\left(1-\nu^2\right)$.

The basic assumption is that the valve motion is made up of a superposition of free vibration modes.

$$w(x,y,t)=\sum_{m=1}^{\infty}\phi_m(x,y)q_m(t) \tag{2.21}$$

Mode shapes $\phi_m(x,y)$ depend on geometry, boundary conditions and valve node position. They are evaluated solving free valve movement by means of a standard FEM program for each frequency m considered.

Participation factors q_m, at each instant and for each frequency m considered, are solved introducing equation (2.21) into the general equation of motion (2.20) and assuming that the vibration at any natural frequency consists on a simple harmonic vibration (i.e., $D\nabla^4\phi\left(x,y\right)=\rho h_v\omega_m^2\phi_m\left(x,y\right)$). Then,

$$\rho h_v\omega_m^2\sum_{m=1}^{\infty}q_m(t)\phi_m\left(x,y\right)+\rho h_v\sum_{m=1}^{\infty}\ddot{q}_m\phi_m\left(x,y\right)=p\left(x,y,t\right) \tag{2.22}$$

Multiplying both sides of equation (2.22) by $\phi_n(x,y)$, taking into account the orthogonality effect of the natural modes (i.e., $\int_s\int\phi_m(x,y)\phi_n(x,y)dS=0$ when $n\neq m$), and integrating over all valve reed surface, the following equation is obtained:

$$\ddot{q}_m(t)+2\xi\omega_m\dot{q}_m(t)+\omega_m^2q_m(t)=\frac{\sum_{i=1}^{ne}\phi_m\left(x_i,y_i\right)p\left(x_i,y_i,t\right)\Delta A_i}{\rho_v h_v\sum_{i=1}^{ne}\phi_m^2\left(x_i,y_i\right)\Delta A_i} \tag{2.23}$$

where damping effect has been introduced in a similar way as eq. (2.19), and ne represents the number of finite elements in which the valve is divided. Considering that force is acting on the valve reed, and flexed in the position of elements j where the valve plate holes are located, effective force area A_F can be defined as:

$$p\left(x_j, y_j, t\right) \Delta A_j = A_F(x_j, y_j) \Delta p(t) \tag{2.24}$$

Introducing equation (2.24) into (2.23) it is possible to obtain the participation factors q_m for each m frequency considered.

$$\ddot{q}_m(t) + 2\xi\omega_m \dot{q}_m(t) + \omega_m^2 q_m(t) = \frac{\Delta p(t) \sum_{j=1}^{nh} \phi_m\left(x_j, y_j\right) A_F(x_j, y_j) \Delta A_j}{A_v \rho_v h_v \sum_{i=1}^{ne} \phi_m^2\left(x_i, y_i\right) \Delta A_i} \tag{2.25}$$

where nh is the number of valve holes. Equation (2.25) is iteratively solved using a fully implicit first order Heun method.

When a more complex valve system is considered, such as a discharge valve with a spring valve, this auxiliary valve is considered as a spring loaded ring valve and equation (2.19) of one degree of freedom valve motion model is used. In this case, the equation of motion (2.25) should consider an extra force term due to the composed valve.

2.5 Instantaneous compression chamber volume evaluation

Compression chamber volume is changing along the time and basically due to the instantaneous piston position, which depends on the force balance among gas pressure in the compression chamber, electrical motor torque, and crankshaft connecting rod mechanical system. compressor driving mechanism geometry is shown in Fig. 2.5.

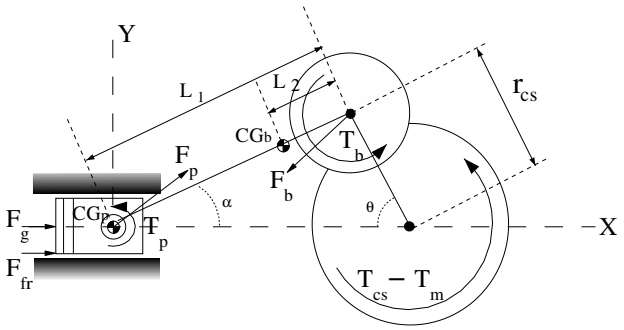

Figure 2.5: Crankshaft connecting rod mechanism force scheme.

The kinematics equation derived from the compressor driving mechanical system is as follows:

$$\ddot{x}_{CGp} = (r_{cs}\cos\theta + A_1)\,\dot{\theta}^2 + (r_{cs}\sin\theta + A_2)\,\ddot{\theta} \tag{2.26}$$

$$\ddot{x}_{CGb} = \left(r_{cs}\cos\theta + \frac{L_2}{L_1}A_1\right)\dot{\theta}^2 + \left(r_{cs}\sin\theta + \frac{L_2}{L_1}A_2\right)\ddot{\theta} \tag{2.27}$$

$$\ddot{y}_{CGb} = -r_{cs}\sin\theta\left(1 - \frac{L_2}{L_1}\right)\dot{\theta}^2 + r_{cs}\cos\theta\left(1 - \frac{L_2}{L_1}\right)\ddot{\theta} \tag{2.28}$$

$$\ddot{\alpha} = \frac{r_{cs}\sin\theta\cos\theta}{\left(L_1^2 - r_{cs}^2\sin^2\theta\right)^{3/2}}\dot{\theta}^2 - \frac{r_{cs}\sin\theta}{\sqrt{L_1^2 - r_{cs}^2\sin^2\theta}}\dot{\theta}^2 + \frac{r_{cs}\cos\theta}{\sqrt{L_1^2 - r_{cs}^2\sin^2\theta}}\theta \tag{2.29}$$

where

$$A_1 = \frac{r_{cs}^2(\cos^2\theta - \sin^2\theta)}{\sqrt{L_1^2 - r_{cs}^2\sin^2\theta}} + \frac{r_{cs}^4\cos^2\theta\sin^2\theta}{\left(L_1^2 - r_{cs}^2\sin^2\theta\right)^{3/2}} \tag{2.30}$$

$$A_2 = \frac{r_{cs}^2\cos\theta\sin\theta}{\sqrt{L_1^2 - r_{cs}^2\sin^2\theta}} \tag{2.31}$$

Evaluating the pressure in the compression chamber at each time-step, and knowing experimentally motor torque vs. frequency, it is possible to evaluate the instantaneous crank angle acceleration $\ddot{\theta}$, together with force between piston and connecting rod $\vec{F_p}$ and force between crankshaft and connecting rod $\vec{F_b}$ by means of force balances on the piston, on the connecting rod and on the crankshaft mechanical system.

The equations presented below show the force and momentum free solid balances on the crankshaft connecting rod mechanical system presented in Fig. 2.5.

$$F_g + F_{fr} - F_{px} = (m_p + m_{wp})\,\ddot{x}_{CGp} \tag{2.32}$$

$$F_{px} - F_{bx} = m_b\ddot{x}_{CGb} \tag{2.33}$$

$$F_{py} - F_{by} = m_b\ddot{y}_{CGb} \tag{2.34}$$

$$F_{px}\left(1-\frac{L_2}{L_1}\right)r_{cs}\sin\theta - F_{py}\left(1-\frac{L_2}{L_1}\right)\sqrt{L_1^2-r_{cs}^2\sin^2\theta} + F_{bx}\frac{L_2}{L_1}r_{cs}\sin\theta \\ -F_{by}\frac{L_2}{L_1}\sqrt{L_1^2-r_{cs}^2\sin^2\theta} + T_p - T_b = I_b\ddot{\alpha} \tag{2.35}$$

$$-F_{bx}r_{cs}\sin\theta - F_{by}r_{cs}\cos\theta - T_m + T_{cs} + T_b = -I_{cs}\ddot{\theta} \tag{2.36}$$

The resulting algebraic system of equations is solved using a direct LU method, which allows to obtain the instantaneous angular acceleration and forces (F_{px},F_{py},F_{bx} and F_{by}). Instantaneous angular velocity $\dot{\theta}$ and crank angle position θ are obtained from the instantaneous angular acceleration $\ddot{\theta}$ using the Adams-Hamilton second order fully implicit method.

Based on crank angle position, piston position x_{CGp} and compression chamber volume V can be finally evaluated.

2.6 Solid walls and oil temperature evaluation

The detailed simulation of the refrigerant gas through the compressor must also be coupled with the thermal behaviour of the surrounding solid elements (shell, muffler, tubes, crankcase, cylinder head, motor, etc.) and the oil. If it is assumed that the oil movement is completely known, the different parts of the compressor are able to be divided into different macro volumes inter-related among them (see the schematic representation in Fig. 2.6).

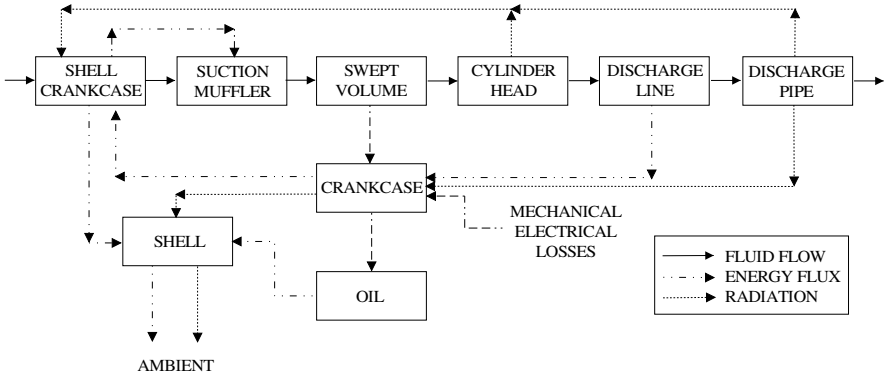

Figure 2.6: Macro volumes energy balance scheme.

For each one of these macro-volumes, the following fully implicit discretized energy equation can be applied, considering convection between solid k and fluid i, and both conduction and radiation between solid k and its neighbours solids j:

$$\begin{aligned}\frac{\rho_k^{n-1}\bar{c}_{pk}\left(T_k^n - T_k^{n-1}\right)V_k}{\Delta t^*} &= \sum_j \frac{T_k^n - T_j^n}{R_{kj}} A_{kj} \\ &+ \sum_i \dot{Q}_{ki}^{conv,n} + \sum_j \dot{Q}_{kj}^{rad,n}\end{aligned} \tag{2.37}$$

The first term on the right hand side corresponds to the conduction heat flux between the elements k and j. The second term represents the convection heat exchange between solid element k and the adjacent fluid i. The third term is the radiation exchange between the solid k and other elements j in the system.

For example, the heat radiation between motor and shell is estimated as:

$$\dot{Q}^{rad,n} = \frac{\sigma(T_{motor}^4 - T_{shell}^4}{\frac{1}{\epsilon_{motor}} + \frac{A_{motor}}{A_{shell}}\left(\frac{1}{\epsilon_{shell}} - 1\right)} A_{motor} \tag{2.38}$$

Time integration can be performed using the same time-step as the fluid ($\Delta t^* = \Delta t$). However, time scales for the solid elements are usually much larger than for the fluid flow. Then, larger time-steps are advisable (specially if multidimensional models are used) to reduce computational cost. In general, the time-steps used in the simulation are of the same order as the cycle time, i.e., $\Delta t^* \approx 1/(\bar{f} n_{\Delta_t})$.

The discretized set of energy equations for the solid elements and oil is linearized and directly solved by an inverse matrix system LU resolution.

2.7 Initial and boundary conditions

At the initial instant, the gas flow pressure, velocity and temperature distribution along all compressor CVs, together with both solid elements and oil temperatures, must be specified.

The gas flow boundary conditions depend on the whole refrigeration system characteristics and operating conditions. The inlet time-averaged gas pressure and temperature, p_{in}, T_{in}, and the outlet time-average gas pressure, p_{out}, must be specified. The relative large volume situated between the shell and the motor-compressor unit damps the gas pulsation induced in the suction line, so the inlet stagnation pressure has been assumed as constant. At the compressor outlet the gas flow pressure is strongly affected by gas pulsations. In this case, pressure is evaluated assuming anechoic boundary conditions, that is, the condenser acts as an infinite pipe in which

the exit waves are completely dissipated [6]. Zero gradient along the flow direction is assumed for the inlet and outlet velocity and outlet temperature. In summary, equations (2.39) (2.40) represent inlet and outlet gas flow section boundary conditions respectively.

$$p = p_{in} - \rho v^2/2 \qquad T = T_{in} \qquad \partial v/\partial x = 0 \tag{2.39}$$

$$p = p_{out} - \rho c\,(v - \bar{v}) \qquad \partial T/\partial x = 0 \qquad \partial v/\partial x = 0 \tag{2.40}$$

where the over-bars denote time-average and x represents the coordinate in the flow direction.

Other boundary conditions are the temperature and pressure of the ambient air and the heat conduction flux through the inlet and outlet connecting pipe to the compressor shell. Radiation heat transfer between the compressor shell and the environment is evaluated considering the environment as a black body with a given temperature (in general the ambient temperature).

2.8 Empirical information

The described mathematical formulation needs some closure relations to evaluate local fluid friction pressure drop and heat transfer coefficients. In the momentum equation, the coefficient of frictional pressure drop is evaluated using standard correlations for flows inside tubes, as Churchill's equation [7]. When singularities are present, the contraction coefficient are evaluated using the classical values of Weisbach cited on [8]. The coefficients needed for the evaluation of the effective flow area are also estimated using the Weisbach's contraction coefficients.

When gas flows at the inlet compressor cross section do not go directly to the suction muffler (see Fig. 1.1), because the inlet shell orifice and the inlet muffler one are not closely connected. Then, a part of the gas goes directly to the inlet suction muffler while the rest is recirculating in the space between the shell and the crankcase. The direct gas mass fraction from the inlet compressor to the suction muffler is considered in this model as input data. This value is experimentally approximated considering Meyer [9] and Cavallini et al. [10] values.

Inside mufflers and tubes the heat transfer coefficients are evaluated using standard empirical correlations for forced convection referenced by Padhy and Dwivedi [11] and Wong [12].

The convective heat transfer coefficient proposed by Liu and Zhou [13] has been employed inside the compression chamber. The heat transfer coefficients between the shell and the environment are the same used by Meyer [9]. The oil energy balance and the mechanical and electrical heat transfer losses are considered in the same manner

as Cavallini et al. [10]. The overall heat transfer coefficients corresponding to the external suction muffler, external cylinder head wall, external crankcase wall together with internal shell wall and external discharge tubes walls are based on Meyer [9] and Fagotti et al. [14], with values ranging between $50 W/m^2$K and $200 W/m^2$K.

Empirical information to evaluate valve motion is basically damping coefficient considered [15]. In one-dimensional model, stiffness also has to be empirically introduced.

The empirical inputs in the crankshaft vs. connecting rod force balances are the friction coefficients between cylinder piston, crankshaft piston pin, crankshaft connecting rod and bearings, with values ranging between 0.007 and 0.2 [16]. It is also necessary to specify the motor electrical efficiency of the selected motor as a function of the instantaneous angular velocity and motor temperature. In this way, the motor torque and the electrical power consumption can be related.

Finally, local thermodynamic and transport properties for different refrigerant fluids and mixtures are evaluated as a function of both temperature and pressure by means of the REFPROP properties program [17].

2.9 Numerical procedure

The whole set of discretized equations describe in the previous section is iteratively solved, at each time-step, by means of a segregated algorithm.

Fluid flow equations are solved by means of a pressure based algorithm of the SIMPLE like (Semi Implicit Method for Pressure Linked Equations) [5] [18] extended to compressible flow. At each grid node, temperature and density are obtained from the discretized energy equation and the state equation respectively. Velocities are calculated at their staggered locations from the discretized momentum equation, together with the equation for the singularity (duct, cavity or valve) when it is presented. Pressures are computed at the grid nodes using a pressure correction equation. This equation is obtained from the continuity equation (2.13) using both a corrected velocity $v'_s = K_v \Delta p'$ and a corrected density $\rho' = K_\rho p'$, where p' is the corrected pressure, $\Delta p'$ is the difference of p' between the adjacent grid nodes and the coefficients K_v and K_ρ are obtained from the discretized momentum equation and state equation respectively. All thermo-physical properties are evaluated at their local conditions.

To solve the momentum equation it is necessary to know the valve position at each time-step considered. The valve dynamic model is applied inside the momentum subroutine, as an iterative loop, to obtain $(KS)_s$, the effective flow area and the valve displacement (see paragraph 2.4). At each instant the compression chamber volume is evaluated based on motor torque force balances, as is described in paragraph 2.5.

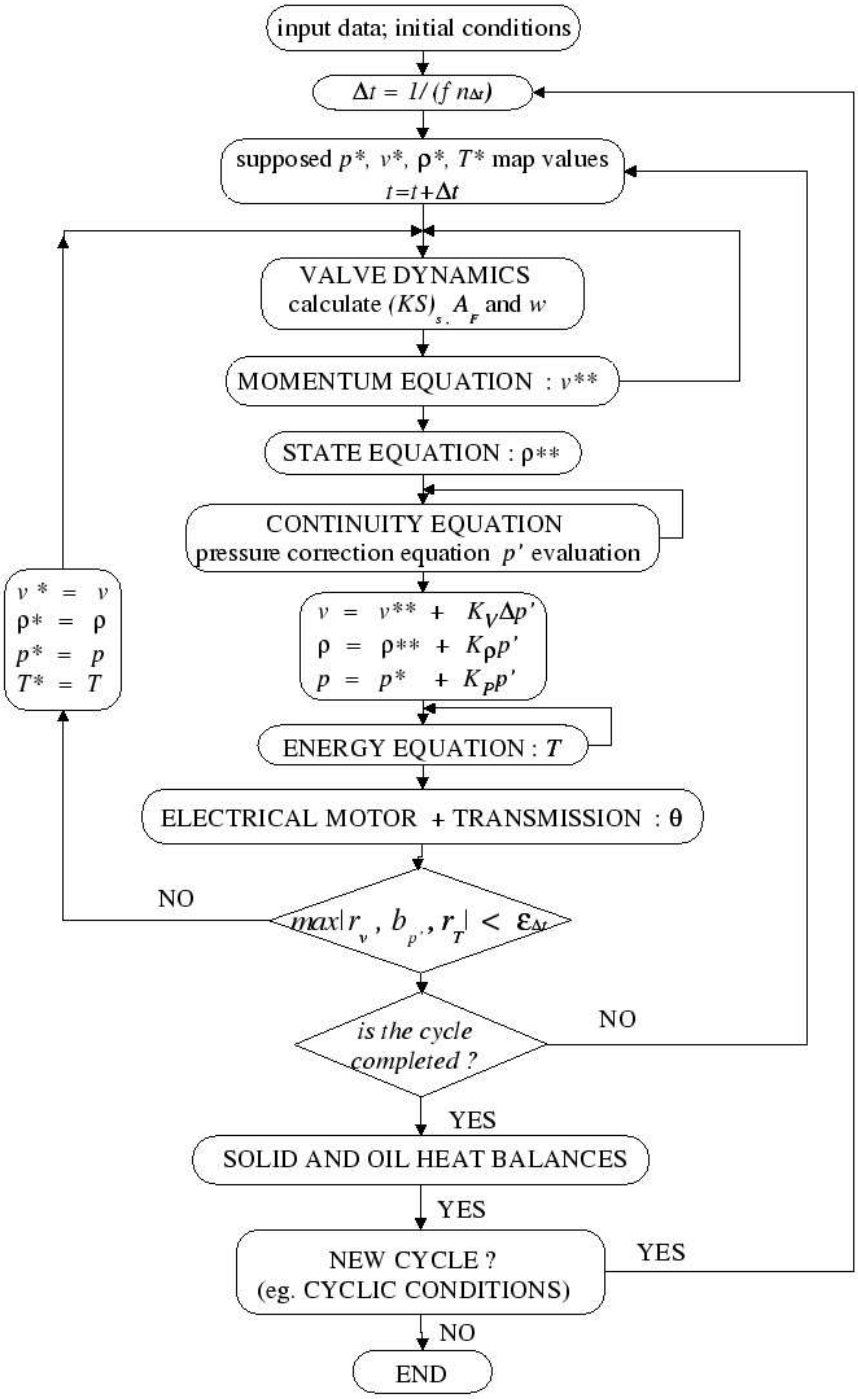

Figure 2.7: General algorithm.

Solid walls and oil temperatures can be evaluated using the same gas flow time-steps, although this is not necessary due to the large differences on time scales of these phenomena. Significant savings in computational time keeping accuracy have been obtained when both solid walls and oil temperatures are calculated only once per cycle using the procedure indicated in paragraph 2.6.

For each time-step, and from guessed values of the different independent variables (usually taken from the previous instant), $(KS)_s$, A_F and ω are calculated from the valve dynamic model. After that, velocities and densities are obtained from the discretized momentum equation and from the state equation respectively. Then, the pressure correction equation is solved and after that pressures, velocities and densities are updated. Temperatures of the refrigerant flow are obtained from the discretized energy equation. Finally, instantaneous angular velocity, motor torque and motor resistance are calculated from the electrical motor subroutine.

The process runs step by step in the time direction giving the transitory evolution of the different variables. Better convergence rates have been obtained when velocities are substituted by a modified velocity, defined as $v^* = vS/S^*$, where the cross-sectional area S^* is an arbitrary reference area. In this manner, the step changes produced in the velocity due to the cross-sectional variations are reduced.

For each time-step, several iterations have to be carried out until convergence is reached. From the momentum equation a residual value r_v is obtained. The continuity equation has an iterative loop until the pressure correction value obtained differs less than the desired accuracy. Finishing the iterative loop, the maximum independent term $b_{p'}$ is kept. From the energy equation another residual value r_T is obtained. Finally, the maximum non-dimensional value between r_v, $b_{p'}$ and r_T has to be less than the selected accuracy $\epsilon_{\Delta t}$ for convergence.

After a complete cycle is run, solid wall and oil temperatures are updated. Usually, the process is not stopped until transitory cyclic conditions are reached, that is, when all fluid flow variables, electrical motor data and solid and oil temperatures from last cycle differs less than converge cycle accuracy ϵ desired.

A schematic representation of the proposed segregated algorithm is presented in Fig. 2.7.

It is possible to perform the computations using known values of the solid walls and oil temperatures and/or a prescribed frequency. In this case, the algorithm runs much faster.

It is worth while to mention that when the motor torque balance is implemented, the real mean frequency is not an input data but an output data of the model.

2.10 Numerical results

The numerical results presented are focused on the quality of the numerical solution by means of a critical analysis of the different numerical sources of errors: convergence errors, discretization errors, programming errors, etc. The accuracy of the mathematical model developed (modelling errors) is presented in next chapter 3.

Numerical simulations have been carried out in PCs with AMD-K7 processors working at 900 MHz. Software code language is FORTRAN 95 and intrinsic variables are type double precision 8 bites.

All cases presented in this section correspond to Electrolux - Unidad Hermética commercial hermetic reciprocating compressor of 7.5 cm^3 of cylinder capacity, working with R134a and a nominal frequency of 50 Hz. Fig. 2.1 corresponds to a schematic representation of the selected compressor without resonator in the discharge line. Table 2.1 presents more significant parameters of the numerically tested compressor.

compression chamber			motor		
cylinder diameter	24.29	mm	crank radius	7.97	mm
clearance ratio	1.55	%	connecting rod length	40.46	mm
suction valve			**discharge valve**		
valve stop	-		valve stop	0.52	mm
first frequency	269.2	Hz	first frequency	325.2	Hz
suction port			**discharge port**		
diameter	7.2	mm	diameter	5.4	mm

Table 2.1: Compressor geometry parameters.

Based on the same experimental studies, the direct gas mass fraction from inlet compressor to suction muffler has been estimated about 30 %. The heat transfer coefficients in the compressor unit surfaces and the internal shell have been considered constant and equal to 150 W/m^2K. The empirical friction coefficient between cylinder and piston has been considered equal to 0.05, while the rest of friction coefficients has been considered equal to 0.02. Fig. 2.10 shows electrical motor efficiency and motor torque vs. frequency respectively as motor curve characterization.

All numerical experiments have been performed assuming a single stage vapour compression low pressure cycle at the following considerations: both inlet compressor temperature and outlet condenser temperature of 32^{o}C, condensation temperature of

55^{o}C and evaporation temperature of -23.3^{o}C. Ambient temperature is fixed at 32^{o}C.

The software developed has been carefully verified to avoid programming errors. Some compressor parts (fluid through tubes or inside compressor chamber) have been tested separately. Conservation of both mass and energy in the whole compressor domain is always accomplished.

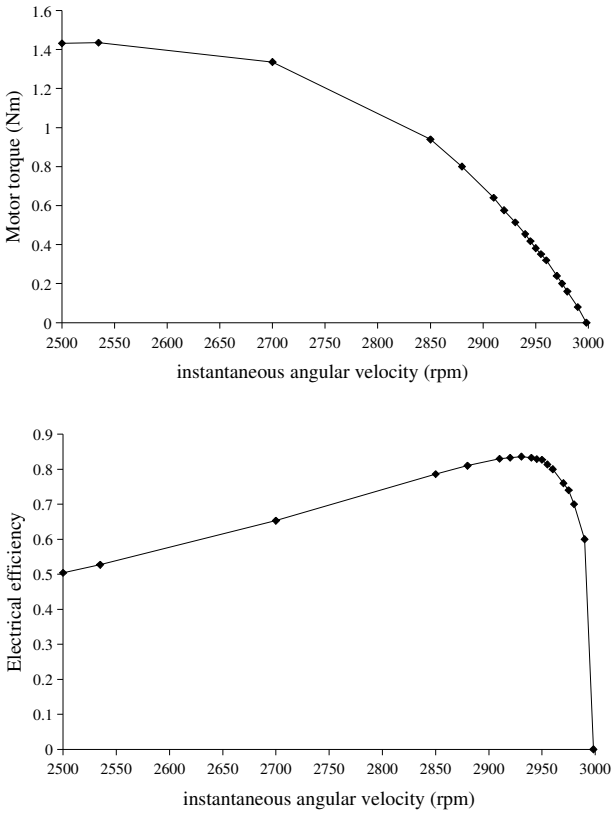

Figure 2.8: Experimental electrical efficiency and motor torque vs. frequency for motor studied.

Compressor behaviour is characterized by the following variables: mass flow rate $\dot{m}$; compression work per unit mass w_{cp}; compressor heat exchanged per unit mass q_{cp}; mean outlet fluid compressor temperature T_{out}; and mean real compressor working frequency when instantaneous compression chamber volume is evaluated.

The majority of these values are also presented in a non-dimensional form by the following parameters: volumetric efficiency $\eta_v = \dot{m}/(\rho_{in} V_{cl} \bar{f}_n)$, isentropic effi-

ciency $\eta_s = w_{iso}/w_{cp}$, heat transfer efficiency defined as $\eta_q = (w_{cp} + q_{cp})/w_{cp}$, and COP considered as a non-dimensional form of presenting electrical power consumption $COP = \dot{Q}_{ev}/\dot{W}_e$.

Initial conditions for all studied cases are: uniform pressure in the suction line and equal to the suction pressure; similarly in the discharge line with the discharge pressure; uniform temperature and equal to the suction temperature.

2.10.1 Convergence errors

To evaluate convergence errors, Table 2.2 presents numerical results depending on the convergence criteria considered to advance in the transitory solution (maximum non-dimensional residual values of the different equations must be lower than a prescribed value $\epsilon_{\Delta t}$) and to reach periodic or cyclic conditions (maximum difference of the different variables, in non-dimension form, of the actual cycle and the previous one must be lower than ϵ).

ϵ, $\epsilon_{\Delta t}$	$\dot{m}$ [kg/h]	w_{cp} [kJ/kg]	q_{cp} [kJ/kg]	T_{out} [C]	η_v [%]	η_s [%]	η_q [%]	it/c	cpu/c [s]	nc	t [h]
1.0e-2	3.784	-102.79	-52.90	101.52	60.01	69.04	48.54	5	1.1	684	0.21
1.0e-3	3.779	-102.89	-54.77	101.56	59.94	68.98	46.77	8	1.7	1168	0.55
1.0e-4	3.778	-102.90	-55.04	101.57	59.92	68.97	46.51	11	2.4	1792	1.19
1.0e-5	3.778	-102.90	-55.06	101.57	59.92	68.97	46.50	14	3.0	2322	1.94
1.0e-6	3.778	-102.90	-55.06	101.57	59.92	68.97	46.50	16	3.5	2887	2.81
1.0e-7	3.778	-102.90	-55.06	101.57	59.92	68.97	46.50	18	3.8	3436	3.63

Table 2.2: Numerical results depending on convergence criteria considered.

Results show how global numerical values tend to give an asymptotic solution. They also show the differences between the two non-dimensional convergence criteria of the transitory process ($\epsilon_{\Delta t}$ and ϵ). For example, between 1.e-3 and 1.e-7 differences are around 0.033% in volumetric efficiency η_v, and around 0.014% in isentropic efficiency η_s and around 0.578% in heat transfer efficiency η_q. Differences between 1.e-4 and 1.e-7 are around 0.02% in heat transfer efficiency η_q and less than 0.008% in the rest of variables.

Obviously, the number of iterations per cycle it/c, the CPU time per cycle cpu/c, the number of cycles to reach periodical conditions nc and the total computational time consumption $time$, increase when convergence criteria decreases. Values lower than 1.e-4 shows no significant differences in the numerical results.

2.10.2 Discretization errors

The influence of discretization errors is shown in Tables 2.3, 2.4, 2.5 and 2.6. All these cases have been run up to $\epsilon_{\Delta t}$ and ϵ values equal to 1.e-7.

Table 2.3 presents numerical results depending on the number of time-steps per cycle chosen (from 180 to 1440).

$n_{\Delta t}$	$\dot{m}$	w_{cp}	q_{cp}	T_{out}	η_v	η_s	η_q	it/c	cpu/c	nc	t
	[kg/h]	[kJ/kg]	[kJ/kg]	[C]	[%]	[%]	[%]		[s]		[h]
180	3.768	-102.84	-54.83	101.73	59.76	69.01	46.68	15	1.7	3498	1.65
360	3.778	-102.90	-55.06	101.57	59.92	68.97	46.50	18	3.8	3436	3.63
720	3.780	-102.92	-55.26	101.41	59.95	68.96	46.31	18	6.0	3520	5.87
1440	3.780	-102.95	-55.40	101.30	59.95	68.94	46.19	24	10.0	3558	9.74

Table 2.3: Numerical results depending on number of time-steps per cycle considered.

Results tend to asymptotic solution increasing the number of time-steps considered. Even though time-step independent numerical solution is not obtained with a typical value of 360 time-steps per cycle, its influence on global results is relatively low. Differences between 360 time-steps and 1440 time-steps are around 0.05% in η_v, 0.04% in η_s and 0.66% in η_q, while outlet temperature T_{out} presents differences around 0.26%. Differences between 720 time-steps and 1440 are around 0.1% in T_{out} and 0.26% in η_q, while differences for the rest of variables are less than 0.03%.

$nodes$	$\dot{m}$	w_{cp}	q_{cp}	T_{out}	η_v	η_s	η_q	it/c	cpu/c	nc	t
	[kg/h]	[kJ/kg]	[kJ/kg]	[C]	[%]	[%]	[%]		[s]		[h]
3	3.778	-102.90	-55.06	101.57	59.92	68.97	46.50	18	3.8	3436	3.63
9	3.778	-102.90	-57.22	99.61	59.92	68.97	44.39	18	4.6	3442	4.40
15	3.778	-102.90	-58.06	98.84	59.92	68.97	43.58	18	5.5	3441	5.26
21	3.778	-102.90	-58.47	98.43	59.92	68.97	43.18	21	7.3	3441	6.98
27	3.778	-102.90	-58.60	98.33	59.92	68.97	43.05	29	10.7	3440	10.2

Table 2.4: Numerical results depending on discharge tube density mesh considered.

Table 2.4 presents different results depending on number of CVs considered in the discharge tube. When the number of grid nodes increases more than 21 CVs, the solution tends to an asymptotic result. Differences between 21 and 27 CVs are lower than 0.1% in T_{out} and less than 0.3% in η_q, while the rest of variables present no

relevant differences. CPU time per cycle cpu/c increases around 30% from 21 nodes to 27 nodes.

Tables 2.5 and 2.6 present different results to evaluate the time-steps per cycle needed to obtain time-step independent results considering instantaneous angular velocity influence (i.e., frequency is not an input data but a consequence of the crankshaft and connecting rod force balances evaluation).

$n_{\Delta t}$	$\dot{m}$ [kg/h]	w_{cp} [kJ/kg]	q_{cp} [kJ/kg]	T_{out} [C]	$\bar{f}$ [Hz]	η_v [%]	η_s [%]	η_q [%]	COP
180	3.718	-102.09	-54.23	101.59	49.22	58.97	69.52	46.88	1.352
360	3.724	-102.20	-54.50	101.43	49.22	59.06	69.44	46.67	1.352
720	3.729	-102.16	-54.72	101.20	49.22	59.14	69.47	46.44	1.351
1440	3.729	-102.20	-54.79	101.16	49.22	59.14	69.44	46.39	1.351

Table 2.5: Numerical results considering instantaneous angular velocity influence.

$n_{\Delta t}$	it/c	cpu/c [s]	nc	$time$ [h]
180	22	2.9	3537	2.85
360	24	6.3	3477	6.08
720	24	12.1	3732	12.54
1440	24	18.3	3460	17.59

Table 2.6: Numerical aspects considering instantaneous angular velocity influence.

Numerical result differences between 360 time-steps and 1440 are around 0.14% in η_v and around 0.1% in η_s, around 0.6% η_q and around 0.07% in COP. Maximum differences between 720 and 1440 are around 0.04% in η_s, around 0.1% in η_q and less than 0.04% for the rest of variables. In the same manner as Table 2.3, although without a fixed frequency, numerical results tend to have an asymptotic solution in all global values.

For the cases considered, differences to use second order transient schemes instead of first order transient schemes are basically when time-step used is between 180 or 360, where differences are around 0.05% in η_v and around 0.3% in η_s, η_q and T_{out}. Differences for time-steps around 720 or 1440 are less than 0.1% in all variables.

2.11 Conclusions

An advanced numerical simulation of the thermal and fluid dynamic behaviour of hermetic reciprocating compressors has been presented. The mathematical model is based on fundamental principles (conservation laws), although some empirical inputs are needed in order to describe fluid-solid interaction and some fluid flow three dimensional effects (local heat transfer coefficient and friction factors, pressure drop coefficients, etc.). The quality of the numerical solution has been assessed by means of a critical analysis of the different numerical sources of errors (convergence errors, discretization errors and programming errors). The results make clear the influence of different numerical parameters: time-step, transient order schemes, number of grid nodes, etc. in order to obtain solutions not dependent on the numerical parameters chosen. The accuracy of the mathematical model developed (modelling errors) is verified in next chapter 3 by means of a comprehensive experimental validation.

2.12 Nomenclature

A	heat transfer area
A_F	effective force area
A_v	valve area
a_P, a_{nb}, b_P	discretization coefficients
$\vec{b}$	body force per unit mass
C	viscous damping factor
C_c	contraction coefficient
COP	coefficient of performance
c_p	specific heat capacity at constant pressure
c_v	specific heat capacity at constant volume
E	Young modulus
e_c	kinetic energy per unit mass
F	force between two solid bodies
F_s	force in flow direction
f	friction factor
$\bar{f}_n, \bar{f}$	nominal and real mean frequency
h	specific enthalpy
h_v	valve height
I	inertia moment
(KS)	effective flow area
L_1	connecting rod length
L_2	crank pin CG connecting rod distance
m	mass
m_p	piston mass
m_{wp}	piston pin mass
m_v	valve mass
$\dot{m}$	mass flow rate
nc	number of cycles
n_{Δ_t}	number of time-steps per cycle
P	chamber perimeter
p	absolute pressure
$\dot{Q}_w$	input control volume heat flux
q_{cp}	compressor heat exchanged per unit mass
q_m	participation factors of mode shapes valves
$\dot{q}_v$	internal heat generation per unit volume
$\vec{\dot{q}}$	heat flux per unit surface
R	contact thermal resistance
r	crankshaft radius
S	surface

T_{dst}	dead state temperature
T_m	motor torque
T	temperature
t	time
u	specific internal energy
$\vec{v}$	fluid velocity
V	volume
V_{cl}	compressor volume displacement
w_{cp}	compression work per unit mass
w	mean valve displacement

Greek symbols

α	convective heat transfer coefficient
α_{rad}	radiation heat transfer coefficient
β	volume expansion coefficient
γ	isentropic coefficient (c_p/c_v)
ΔA_i	finite element valve area
Δp	instantaneous mean pressure difference
Δt	time-step
Δz	length
ϵ	convergence criteria to reach cyclic conditions
$\epsilon_{\Delta t}$	maximum residual allowed at each Δt
η_q	heat transfer efficiency
η_s	isentropic efficiency
η_v	volumetric efficiency
θ	connecting rod piston angle position
ν	coefficient of Poisson
ξ	damping coefficient
ρ	fluid density
ρ_v	valve density
σ	cross sectional area ratio
$\vec{\sigma}$	stress tensor
ϕ_m	natural valve mode shapes
ϕ	generic variable
ω_n	natural frequency

Subscripts

CG	center of mass
cc	crankshaft crank pin
cp	connecting rod piston pin

cr	connecting rod
cs	crankshaft
fr	friction
g	gas
i	inlet cross section
nb	control volume neighbour nodes
o	outlet cross section
P	control volume central node

Superscripts

n	current time instant

References

[1] Z.U.A. Warsi. *Fluid Dynamics, Theoretical and Computational Approaches*. CRC Press, Inc., 1993.

[2] P.M. Morse and H. Feshbach. *Methods of Theoretical Physics, Part II*. McGraw-Hill Book Company, NY, 1953.

[3] W.B. Brower, E. Eisler, E.J. Filkorn, J. Gonenc, C. Plati, and J. Stagnitti. On the compressible flow through an orifice. *Journal of Fluid Engineering*, 115:660–664, 1993.

[4] D.D. Schwarzler and J.F. Hamilton. An analytical method for determining effective flow and force areas for refrigerating compressor valving system. In *International Compressor Engineering Conference*, pages 30–36, Purdue University, IN, USA, 1972.

[5] S.V. Patankar. *Numerical Heat Transfer and Fluid Flow*. McGraw-Hil, NY, USA, 1980.

[6] W. Soedel. *Mechanics, Simulation and Design of Compressor Valves, Gas Passages and Pulsation Mufflers*. Purdue University Short Courses, IN, USA, 1992.

[7] S.W. Chuchill. Friction equation spans all fluid flow regimes. *Chemical Engineering*, 84:91–99, 1977.

[8] V.L. Streeter and E.B. Wylie. *Fluid Mechanics*. Mc-Graw Hill, 8th ed, N.Y., USA, 1985.

[9] W.A. Meyer. *An investigation into heat transfer processes in a small hermetic refrigeration compressor*. PhD thesis, Purdue University, Indiana, USA, 1987.

[10] A. Cavallini, L. Doretti, G.A. Longo, L. Rosseto, B. Bella, and A. Zanneiro. Thermal analysis of a hermetic reciprocating compressor. In *International Compressor Engineering Conference*, pages 535–540, Purdue University, IN, USA, 1996.

[11] S.K. Padhy and S.N. Dwivedi. Heat transfer analysis of a rolling-piston rotary compressor. *International Journal of Refrigeration*, 17(6):400–410, 1994.

[12] H.Y. Wong. *Handbook of essential formulae and data on heat transfer for engineers*. Longman, NY, USA, 1977.

[13] R. Liu and Z. Zhou. Heat transfer between gas and cylinder wall of refrigerating reciprocating compressor. In *International Compressor Engineering Conference*, pages 110–115, Purdue University, IN, USA, 1984.

[14] F. Fagotti, M.L. Todescat, R.T.S. Ferreira, and A.T. Prata. Heat transfer modelling in a reciprocating compressor. In *International Compressor Engineering Conference*, pages 605–610, Purdue University, IN, USA, 1994.

[15] K.T. Ooi and G.B. Chai. A simple model to study the performance of a small compressor. In *International Compressor Engineering Conference*, pages 147–156, Purdue University, IN, USA, 1992.

[16] J.E. Shigley and C.R. Mischke. *Mechanical Engineering Design.* 5th ed., McGraw-Hill, New York, 1990.

[17] National Institute of Standards and Technology. Nist thermodynamic and transport properties of refrigerants and refrigerant mixtures - refprop version 6.01. Gaithersburg, MD, USA, 1998.

[18] J.P. Van Doormal, G.D. Raithby, and B.H. McDonald. The segregated approach to predicting viscous compressible fluid flows. In *International Gas Turbine Conference Exhibit*, pages 86–GT–196. ASME paper, 1986.

Chapter 3

Experimental investigation

3.1 Introduction

An experimental validation of the mathematical model developed for the numerical simulation of the thermal and fluid dynamic behaviour of hermetic reciprocating compressors is presented. Details of the physical model and a critical analysis of the quality of the numerical solution have been presented in the previous chapter 2. Different compressor geometries have been tested considering a wide range of working conditions and refrigerant fluids. A complete description of the experimental equipment and its instrumentation has been performed. Good agreement between numerical and experimental data has been obtained giving a better understanding of the thermal and fluid dynamic behaviour of these compressors.

Global working parameters of hermetic reciprocating compressors have been compared numerically and experimentally on both calorimeter set-up and laboratory set-up. The calorimeter set-up is a standard experimental unit, according to ISO 917 regulations, specially designed to evaluate compressor global working parameters. The laboratory set-up is a specific unit designed and built to research purposes, that is, to validate mathematical models for each one of the components of a single stage vapour compression system (compressor, condenser, expansion device, evaporator) and also for the whole equipment [1] [2] [3]. Both experimental units provide information about compressor inlet and outlet temperatures, mass flow rate, power consumption and cooling capacity. Both inlet and outlet compressor pressures and inlet and ambient temperatures can be controlled for a wide range of working conditions and refrigerant fluids.

A first detailed thermal behaviour comparison has been carried out adapting a commercial hermetic reciprocating compressor of 7.5 cm^3, working with R134a at a nominal frequency of 50 Hz. It has been specially instrumented with 23 thermocouples, collocated in different strategic points, to obtain a detailed information of the wall and fluid temperature map [4] [5] under different pressure conditions.

A second detailed compressor instrumentation has been carried out with a same commercial compressor, although encased in a bigger special shell with three special pressure transducers to measure absolute instantaneous pressure in: suction muffler, compression chamber and cylinder head. An incremental encoder has been connected to crankshaft connecting rod mechanical system to evaluate instantaneous piston position. This second detailed experimental evaluation allows to determinate experimentally pV diagram inside compressor chamber [6].

The objective of this chapter is to present an experimental validation of the numerical simulation model presented above. Both calorimeter and laboratory set-ups are described in detail, together with the hermetic compressor detailed instrumentations. Different fluid refrigerants, compressors capacities, compression ratios and boundary conditions have been tested. The experimental results obtained are compared and contrasted with the numerical results obtained by means of the simulation program. The experimental results obtained has been used also to validate the mathematical model developed and to get better understanding of the thermal and fluid dynamic phenomena involved in these devices.

3.2 Experimental set-up

Experimental data have been obtained in two different set-ups. The first one is hereafter referred as calorimeter test which corresponds to Electrolux calorimeter standard experimental units designed to standard purpose. The second one is hereafter referred as laboratory set-up which corresponds to a particular set-up designed in the CTTC laboratory to research purposes. Both are basically single stage vapour compression refrigerating experimental units that allows to control inlet and outlet compressor pressure, inlet compressor temperature and ambient conditions, together with secondary circuits control.

3.2.1 Calorimeter set-up

Calorimeter set-up, constructed according to ISO 917, basically consists on a single stage vapour compression unit, where the evaporator is suspended in the upper part of a pressure-tight heat-insulated vessel. A heater in the base of this vessel is charged with a volatile secondary fluid. Expansion valve controls refrigerant flow. Secondary fluid through condenser is water. The calorimeter set-up is well-prepared to maintain its ambient temperature constant within $\pm 0.5^o$C.

The fluid flow temperature at each inlet and outlet refrigerating system cross sections are measured, together with evaporator secondary fluid temperatures, by means of thermocouples with a standard deviation of $\pm 0.3^o$C. Thermocouples precision is $\pm 0.2^o$C.

Pressure regulation at inlet and outlet compressor sections are maintained below ±5 mbar and ±0.1 bar respectively. Pressure transducers precision guarantees ±0.2% F.S., which depends on working fluid used. For R134a, inlet and outlet pressure transducers have a range of 10 and 20 bars respectively. For R404A the ranges are 15 and 40 bars, while for R600a ranges are 3 and 20 bars.

Compressor power measurement and electrical heaters measurements are guaranteed within ±1%.

Calorimeter test ISO 917 regulations guarantees mass flow rate and refrigerating capacity accuracy within ±3% and compressor power accuracy within ±1% of values measured.

Based on these considerations, volumetric efficiency, isentropic efficiency and coefficient of performance are able to be evaluated within an accuracy of ±3%, ±3% and ±4% respectively.

3.2.2 Laboratory set-up

An experimental unit has been built to study single stage vapour compression refrigerating systems [1] [2] [3]. This unit has been designed to validate mathematical models of the thermal and fluid dynamic behaviour of single stage vapour compression refrigerating units in general and their elements in particular. Fig. 3.1 shows experimental unit scheme commented above.

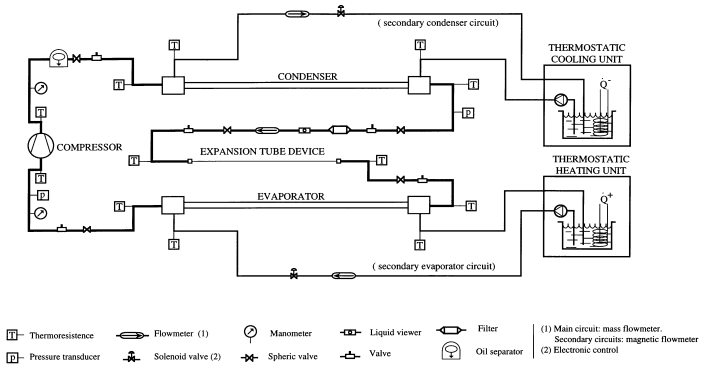

Figure 3.1: Experimental unit general scheme.

Elements that make up the experimental unit are basically: hermetic reciprocating compressor, double-pipe condenser and evaporator, together with an expansion valve. Auxiliary fluid for condenser and evaporator annuls is water.

The fluid flow temperatures inside tubes and annuli are measured with platinum resistance thermometer sensors Pt-100 located at the inlet and outlet sections of each element of the main and secondary circuits and with an accuracy of ±0.15 ±0.002·T ^{o}C.

Transducers from 0-16 bars and 0-6 bars measure condenser and evaporator absolute pressures respectively. Pressure transducers accuracy is within ±0.1% FS. Refrigerant mass flow rate is measured with a Coriolis type mass flow-meter within an accuracy of ±0.0009kg/min.

Two thermostatic heating and cooling units allow controlling inlet auxiliary water temperature at both evaporator and condenser auxiliary circuits respectively. Volumetric flow in these secondary circuits is controlled by two modulating solenoid valves and is measured through two magnetic flow-meters with an accuracy of ±0.01 l/min from 0 to 2.5 l/min and ±0.5% F.S. to 25 l/min.

3.3 Detailed instrumentation of hermetic reciprocating compressor (I)

A commercial hermetic reciprocating compressor has been instrumented with 23 thermocouples to obtain a detailed experimental temperature compressor map.

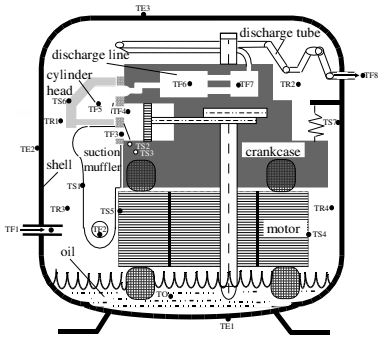

Figure 3.2: Compressor scheme including thermocouples position.

Figure 3.3: Compressor view including thermocouples group.

Fluid temperatures	
TF1	Inlet compressor
TF2	Inlet suction muffler
TF3	Suction orifice
TF4	Discharge orifice
TF5	Cylinder head
TF6	Discharge chamber 1
TF7	Discharge chamber 2
TF8	Outlet compressor

Solid and oil temperatures	
TS1	Muffler wall
TS2	0.5 mm far from compressor cylinder
TS3	1 mm far from compressor cylinder
TS4	External motor crankcase wall
TS5	External crankcase wall near muffler
TS6	Solid cylinder head
TS7	Internal shell wall
TO	Oil temperature

Remnant fluid temperatures	
TR1	Remnant gas top
TR2	External remnant gas top
TR3	Remnant gas middle
TR4	Remnant gas middle

External solid temperatures	
TE1	External bottom shell wall
TE2	External middle shell wall
TE3	Top shell wall

Table 3.1: Compressor thermocouples location.

Twenty K type thermocouples, of 0.5 mm diameter, have been built in four groups with five thermocouples in each group. Each thermocouple is encapsulated inside a thin steel stick, and the wires are electrically insulated with MgO. Four holes have been screwed in the compressor shell to pass through them the different groups, by means of vacuum pressure feedthroughs.

The other three thermocouples are also K type and they are only covered with a steel grid. These thermocouples measure the external shell wall temperature.

As is indicated in Table 3.6, the different thermocouples have been positioned to measure fluid flow temperatures through different strategic points along compressor circuit: TF1-TF3 for suction line, TF4-TF8 for discharge line and TR1-TR4 for mean remnant fluid temperature between crankcase and shell. The other thermocouples have been located to measure internal wall temperature of different solid elements: TS1 for muffler wall, TS2-TS3 for internal crankcase, TS4-TS5 for external crankcase, TS6 for cylinder head and TS7 for internal shell wall. Mean external compressor shell temperature, TE1- TE3, together with oil temperature, TO, are also measured. Figs. 3.2 and 3.3 show compressor view and compressor scheme with the different thermocouple locations.

Fig. 3.4 shows the compressor with lid off and instrumented with all the internal thermocouples and vacuum feedthroughs. Fig. 3.5 shows thermocouples through different solid parts and between shell and crankcase.

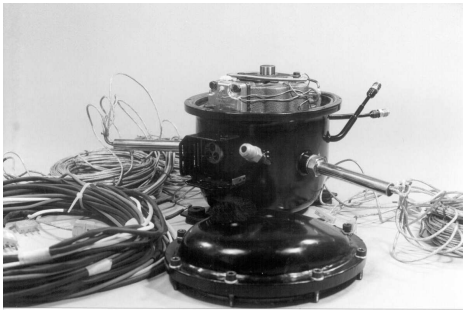

Figure 3.4: General compressor view opened.

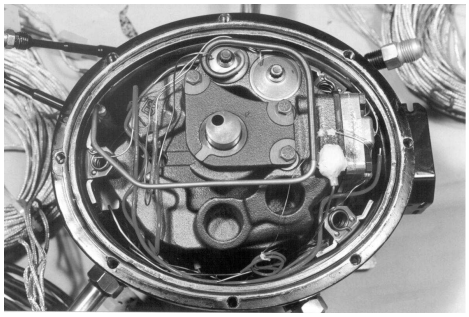

Figure 3.5: General compressor top view with thermocouples.

Fig. 3.6 shows in detail two thermocouples through the cylinder head wall to measure fluid flow temperature inside this chamber together with one thermocouple in suction plenum to measure fluid flow temperature through suction orifice. Same picture shows one thermocouple in valve plate through discharge hole. Fig. 3.7 shows several thermocouples positions at the top crankcase zone: fluid temperature between shell and crankcase, fluid temperature inside cylinder head and wall cylinder head and crankcase temperatures.

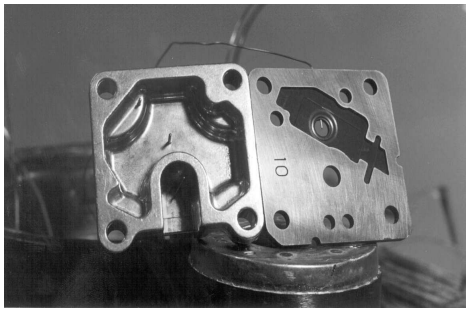

Figure 3.6: Cylinder head and valve plate details.

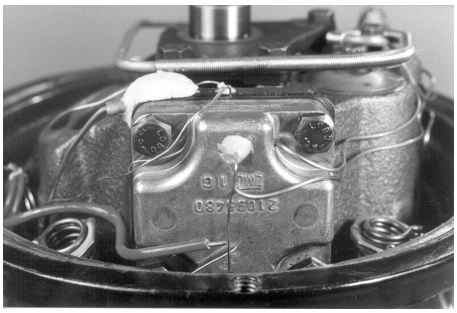

Figure 3.7: Cylinder head and crankcase details.

A precision Platinum Resistance Thermometer (PTR) has been used as the reference value in the thermocouples calibration. The PTR system accuracy is $\pm$ 0.025^{o}C. The Data Acquisition and Control System (DACS) used guarantees an accuracy of $\pm$ 0.35^{o}C, while internal isothermal reference temperature blocks in DACS are between 23^{o}C $\pm$ 0.5^{o}C. After calibration, the K-type thermocouples have an accuracy of $\pm$ 0.7^{o}C.

3.4 Detailed instrumentation of a hermetic reciprocating compressor (II)

A commercial hermetic reciprocating compressor has been encased in a bigger special shell, in order to keep compressor crankcase and encoder together (see Fig. 3.8).

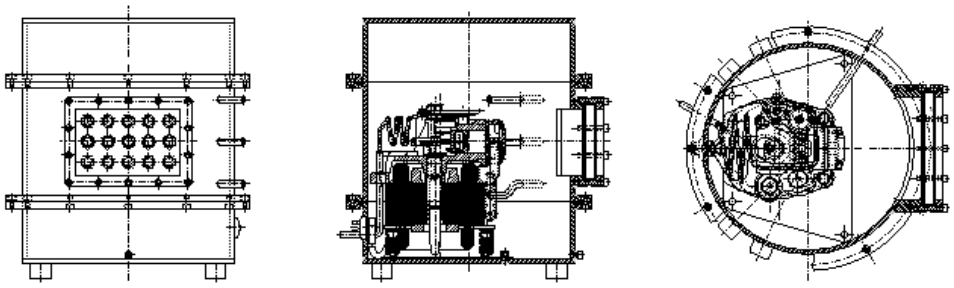

Figure 3.8: Hermetic reciprocating compressor prototype scheme: front, side and top views respectively.

Different K type thermocouples have been put inside compressor to measure fluid temperature distribution along specific points: compressor shell, inlet muffler, discharge tube, wall temperatures, etc. Three special pressure transducers have been introduced to measure: suction muffler, compression chamber and cylinder head absolute fluid pressure. An incremental encoder has been connected to crankshaft connecting rod mechanism to evaluate instantaneous piston position. Fig. 3.9 shows general instrumented compressor view.

A specific Dynamic Analyzer Signal DAC NI PXI 4472 unit has been employed to measure fast variables like pressures and encoder position. A more general purpose Data Acquisition and Control System DACS unit to show variables like single stage vapour compression refrigerating experimental unit temperatures, mass flow rate, etc. is used. This DACS unit also allows controlling pressure ratio work unit and secondary fluids control. Finally, a specific Data Acquisition Switch Unit DASU hp 34970A is used to measure temperatures inside compressor. Fig. 3.10 shows compressor unit with DAS and DASU systems together.

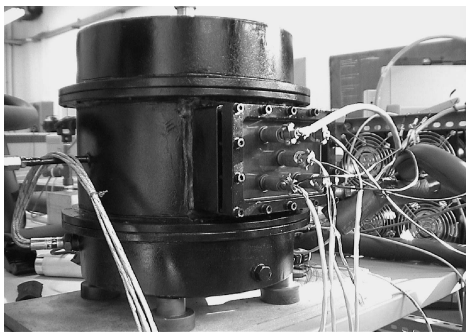

Figure 3.9: General instrumented compressor view.

Figure 3.10: Compressor view with acquisition units.

The instrumentation has been carried out under a commercial hermetic reciprocating compressor. A few changes have been necessary to instrument the compressor. A special piece has been built to connect encoder with connecting rod. Specific holes through cylinder head to connect pressure transducers and several holes through the shell for transducers connections together with temperature groups feedthroughs have also been employed.

A relative quadrature encoder of 720 pulses/revolution with a maximum frequency output of 100kHz has been used to measure instantaneous piston position at each half crank angle degree. From the electrical power consumption, the relative encoder adds losses around 6% of measured power consumption, for the studied cases. Figs. 3.11 and 3.12 show general view encoder position and pressure transducers distribution.

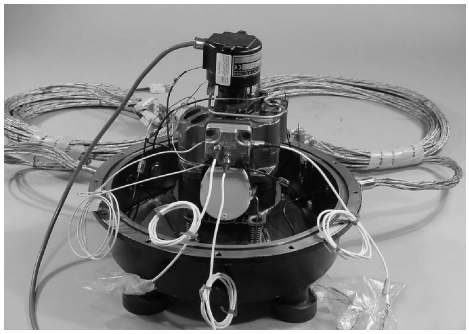

Figure 3.11: Detailed compressor instrumentation.

Figure 3.12: Detailed crankcase instrumentation.

Three piezo-resistive miniature absolute pressure transducers have been introduced to measure the following points: suction pressure at the end of suction muffler, compression chamber pressures under valve plate and discharge pressure inside cylinder head. Figs. 3.13 and 3.14 shows transducers position in detail.

The transducers used are high sensitive, with high natural frequency and thermal compensated between 80 and 160^{o}C. The range is from 0 to 10 bar, although it can works with an overpressure of 2 times F.S. without losing linearity. Then, it has an accuracy of 0.1% F.S. combining non-linearity and hysteresis.

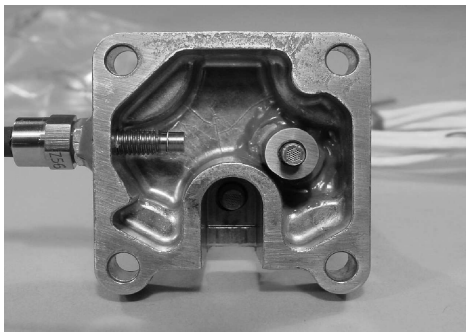

Figure 3.13: Pressure transducers inside cylinder head.

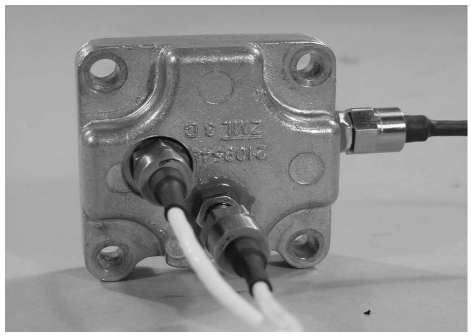

Figure 3.14: Pressure transducers outside cylinder head.

Calibration and linearity has been certified against precision pressure controller which has an accuracy of 0.003% F.S. and stability of 0.01% F.S. This second calibration has verified that pressure measurements error is lower ± 10 mbar from 0 to 20 bars.

Ten internal K type thermocouples have been built in two thermocouple groups with five thermocouples in each group. Thermocouple groups pass through the shell with vacuum pressure feedthroughs. Thermocouples inside the compressor shell are encapsulated with steel, and electrically insulated with MgO between two wires and the steel thin stick. A third pin connects the steel capsulate inside the shell with a steel grid outside the shell and it is connected to the ground.

Thermocouples have been calibrated by means of a thermostatic refrigerating unit working at different temperatures and using mineral oil. A precision Platinum Resistance Thermometer is used as the reference value. Both thermometers have been put together. PTR is read with an individual data acquisition model. The PTR system accuracy is ± 0.025^{o}C. A Data Acquisition Switch Unit DASU used guarantees an accuracy of ± 0.2^{o}C. Thermocouples K type have an accuracy after calibration of ± 0.08^{o}C. Thus, total accuracy temperature measured is less than ± 0.3^{o}C.

3.5 Results

An extensive hermetic reciprocating compressor experimental validation of the mathematical model presented in chapter 1.3 has been carried out. This study has been primarily focused on the different global working parameters using the calorimeter set-up.

The global comparative results allow to check the possibilities of the numerical simulation presented above and its accuracy compared with experimental data.

The mathematical model developed needs different empirical information; part of this information are the local convective heat transfer coefficients between the refrigerant gas and the solid walls. Then, detailed experimental tests of the average temperatures, of both fluid and surfaces in different compressor zones, have been carried out to obtain experimental evidence of these global heat fluxes.

Pressure volume diagram in compression chamber is an important information to compressor development and optimization. Then, detailed experimental tests of the instantaneous pressure in different compressor zones, together with pV diagram inside compression chamber have been carried out to obtain experimental data.

3.5.1 Global working parameters comparison

All compressor results here presented have been tested in the calorimeter set-up described in section 3.2. Numerical simulation is performed according to the mathematical model presented in part 1, and using the following input data information: inlet and outlet mean fluid flow compressor pressure, inlet fluid temperature, compressor geometry, valve dynamic modal analysis, electrical motor characteristic curves, ambient conditions and thermo-physical properties data base [7]. No other data are necessary. However, direct gas mass fraction from inlet compressor to suction muffler is empirically estimated to 30% in all cases and conditions. This value is close to the data considered in [8] and [9] for similar geometrical conditions.

Different cases have been tested for different compressor capacities between 7.5 cm^3 and 16 cm^3, at different compression ratios (evaporation temperatures from -35.0^{o}C to +7.2^{o}C) and working with different refrigerant fluids like R134a, as more used current refrigerant, R600a, as non-contaminant hydrocarbon refrigerant, and R404A as new refrigerant mixture.

Tables 3.2, 3.3 and 3.4 show different comparative results considering mass flow rate and power consumption, or in a non-dimensional form: volumetric efficiency, $\eta_v = \dot{m}/(\rho_{in} V_{cl} \bar{f}_n)$, and coefficient of performance, $COP = \dot{Q}_{ev}/\dot{W}_e$. For convenience, isentropic efficiency numerically evaluated, $\eta_s = w_{iso}/w_{cp}$, is also shown. In these equations: $\dot{m}$ is the real compressor mass flow rate, ρ_{in} is the inlet compressor fluid density, V_{cl} is the compressor cylinder capacity, $\bar{f}_n$ is the mean nominal compressor working frequency, $\dot{Q}_{ev}$ is the cooling capacity of the system, $\dot{W}_e$ is the compressor

power consumption, w_{cp} is the real compression work per unit mass and w_{iso} is the isentropic work per unit mass.

	7.5 cm^3									
	numerical					*experimental*				
T_{evap}	$\dot{m}$	η_v	$\dot{W}_e$	η_s	COP	$\dot{m}$	η_v	$\dot{W}_e$	η_s	COP
[C]	[kg/h]	[%]	[W]	[%]		[kg/h]	[%]	[W]	[%]	
-10.0	7.64	69.1	204.6	73.4	1.91	7.03	63.6	207	66.7	1.74
-23.3	3.83	60.8	138.9	73.7	1.42	3.58	56.7	143	66.8	1.29
-35.0	1.44	39.3	83.3	68.8	0.89	1.54	42.1	93	66.0	0.86
	9.0 cm^3									
	numerical					*experimental*				
T_{evap}	$\dot{m}$	η_v	$\dot{W}_e$	η_s	COP	$\dot{m}$	η_v	$\dot{W}_e$	η_s	COP
[C]	[kg/h]	[%]	[W]	[%]		[kg/h]	[%]	[W]	[%]	
-10.0	10.36	75.7	293.6	71.2	1.81	9.51	69.5	265.3	72.4	1.83
-23.3	4.86	63.5	185.5	69.8	1.35	4.81	62.8	189.3	67.7	1.31
-35.0	2.17	51.0	121.8	60.4	0.92	2.27	53.3	134.0	57.4	0.88

Table 3.2: Global comparative results with R134a as fluid refrigerant.

	14.0 cm^3									
	numerical					*experimental*				
T_{evap}	$\dot{m}$	η_v	$\dot{W}_e$	η_s	COP	$\dot{m}$	η_v	$\dot{W}_e$	η_s	COP
[C]	[kg/h]	[%]	[W]	[%]		[kg/h]	[%]	[W]	[%]	
-10.0	4.76	74.5	229.8	72.2	1.92	4.60	72.0	226	70.9	1.88
-23.3	2.43	66.0	153.1	69.7	1.48	2.43	66.0	157	67.9	1.44
-35.0	1.10	52.0	96.7	62.5	1.07	1.19	56.2	106	61.7	1.05
	16.0 cm^3									
	numerical					*experimental*				
T_{evap}	$\dot{m}$	η_v	$\dot{W}_e$	η_s	COP	$\dot{m}$	η_v	$\dot{W}_e$	η_s	COP
[C]	[kg/h]	[%]	[W]	[%]		[kg/h]	[%]	[W]	[%]	
-10.0	5.50	75.3	256.6	76.4	1.98	5.15	70.5	242	75.8	1.97
-23.3	2.78	66.2	173.1	72.4	1.50	2.64	62.8	169	70.4	1.45
-35.0	1.24	51.4	110.6	64.0	1.05	1.38	56.9	119	66.3	1.08

Table 3.3: Global comparative results with R600a as fluid refrigerant.

	8.0 cm³									
	numerical					*experimental*				
T_{evap}	$\dot{m}$	η_v	$\dot{W}_e$	η_s	COP	$\dot{m}$	η_v	$\dot{W}_e$	η_s	COP
[C]	[kg/h]	[%]	[W]	[%]		[kg/h]	[%]	[W]	[%]	
+7.2	32.77	72.8	543.3	77.7	2.23	32.63	72.5	550	76.5	2.19
-10.0	15.98	65.4	414.5	77.9	1.39	15.94	65.3	418	77.1	1.38
-25.0	7.67	56.1	296.2	76.5	0.91	7.64	55.5	300	75.2	0.88
	12.0 cm³									
	numerical					*experimental*				
T_{evap}	$\dot{m}$	η_v	$\dot{W}_e$	η_s	COP	$\dot{m}$	η_v	$\dot{W}_e$	η_s	COP
[C]	[kg/h]	[%]	[W]	[%]		[kg/h]	[%]	[W]	[%]	
+7.2	53.28	74.7	835.8	82.2	2.36	53.66	75.2	810	85.4	2.45
-10.0	26.61	68.7	622.6	78.8	1.55	26.53	68.5	617	79.3	1.56
-25.0	12.95	59.7	434.3	73.9	1.04	12.52	57.7	449	69.2	0.97

Table 3.4: Global comparative results with R404A as fluid refrigerant.

All cases presented in Tables 3.2 and 3.3 have been tested working with R134a and R600a respectively, in a range of evaporation temperatures from -35^{o}C to -10^{o}C. Condenser temperature is always kept to 55^{o}C. Inlet compressor temperature, sub-cooling condenser temperature and ambient temperature are kept constant at 32^{o}C.

The cases presented in Table 3.4 have been tested working with R404A within a range of evaporation temperatures from -25^{o}C to +7.2^{o}C. Condenser temperature is always kept to 55^{o}C. Inlet compressor temperature and ambient temperature are 35^{o}C, while sub-cooling condenser temperature are kept constant at 46^{o}C.

The results show that volumetric efficiency numerically predicted is overestimated around 4% at high evaporation temperatures, from 0.2% to 8.2%, differs around 3% at nominal conditions, from 0.1% to 6.7%, and is underestimated around -7.5% at low evaporation temperatures, from -4.5% to -10.5%.

Discrepancies between numerical results and experimental data in COP are also shown in these Tables. COP numerically predicted is overestimated around 2% at high evaporation temperatures, from -1.6% to 9%, has the maximum difference at nominal conditions around 4.5%, from 1.7% to 9.3%, and it is also overestimated around 2% at low evaporation temperatures, from -3.6% to 5%.

It is interesting to remark that the mathematical model only uses fundamental information of heat transfer coefficients, friction factors and pressure drop through singularities. No ad-hoc coefficients have been used at all.

In order to reduce these discrepancies, some improvements should be introduced in the simulation, specially in valve dynamic models and heat transfer effects. Specific

studies using CFD simulations of the flow through the valves [10] and inside compression chamber are being carried out. Also, multidimensional simulation models and experimental studies should be performed to get a better understanding and more accurate correlations of heat transfer and pressure drop phenomena of pulsating flows through tubes and mufflers.

3.5.2 Detailed comparative results (I)

A first hermetic reciprocating compressor has been instrumented in detail (see paragraph 3.3). Detailed experimental results of the average temperatures of both fluid and solid elements in the most compressor zones have been obtained for different compression ratios. Numerical results are compared with experimental data obtained in all the studied cases, with and without external fan for shell refrigeration.

Tables 3.6 and 3.7 show the experimental temperature maps for fluid flow and solid walls at different compressor locations using both calorimeter set-up and experimental set-up. All cases here presented have been obtained considering the same boundary conditions as the ones established in subsection 3.5.1 for R134a, except ambient temperature in laboratory set-up which has been 30^oC. In both Tables, the two first columns correspond to evaporation temperatures of -10.0^{o}C and -23.3^{o}C using an external fan. The third and fourth columns correspond to evaporation temperatures of -23.3^{o}C and -30.0^{o}C without using any external fan.

Special attention has been focused on heat transfer coefficients and correlations used in the numerical simulation presented in Part 1, with the objective to determine differences between numerical and experimental detailed comparative results and evolutions.

The heat transfer coefficients in the numerical simulation model have been divided in different groups. First group corresponds to the inlet heat transfer coefficients in tubes and chambers inside compressor muffler, crankcase and discharge tube. These coefficients are evaluated using existing standard empirical correlations [11]. The convective heat transfer coefficient in the compression chamber is based on Liu and Zhou correlation [12]. The heat transfer coefficients between the shell and environment are the same used by Meyer [8]. The oil energy balance and the mechanical and electrical heat transfer losses are evaluated according to Cavallini et al. [9]. Final group corresponds to the external suction muffler, external cylinder head wall, external crankcase wall, internal shell wall and external discharge tube walls. For all of them, a constant heat transfer coefficient of 150 W/m^{2}K has been assumed. This value is consistent with the experimental studies of Meyer [8] and Fagotti et al. [13], in which heat transfer coefficients range between 50 W/m^{2}K and 200 W/m^{2}K.

T_{evap}	-10.0†	-23.3†	-23.3	-30.0	T_{evap}	-10.0†	-23.3†	-23.3	-30.0
Fluid temperatures (C)					*Solid and oil temperatures (C)*				
TF1	33.0	33.4	33.0	33.0	TS1	61.4	62.6	82.3	83.0
TF2	54.3	52.9	71.8	69.8	TS2	95.4	91.4	114.8	109.6
TF3	65.2	66.4	86.5	88.3	TS3	93.2	89.7	112.3	102.3
TF4	118.5	124.6	146.1	145.7	TS4	63.8	62.0	88.2	84.9
TF5	122.5	121.3	142.5	135.2	TS5	65.2	63.0	87.2	87.6
TF6	108.4	99.9	122.9	112.2	TS6	111.1	108.8	131.1	124.4
TF7	99.9	91.4	115.0	106.4	TS7	49.8	47.6	72.6	70.5
TF8	79.6	67.5	104.5	97.0	TO	64.3	62.8	88.5	86.9
Remnant fluid temperatures (C)					*External solid temperatures (C)*				
TR1	71.2	70.7	97.6	92.8	TE1	43.5	44.1	74.0	71.6
TR2	69.8	68.3	93.7	91.0	TE2	48.2	47.9	78.3	74.9
TR3	61.7	60.6	83.4	82.0	TE3	48.2	46.3	74.0	71.6
TR4	63.6	62.9	85.9	86.2					

Table 3.5: Instrumented compressor experimental values in calorimeter set-up. † with an external fan

T_{evap}	-10.0†	-23.3†	-23.3	-30.0	T_{evap}	-10.0†	-23.3 †	-23.3	-30.0
Fluid temperatures (C)					*Solid and oil temperatures (C)*				
TF1	24.5	26.0	26.3	27.7	TS1	55.4	56.3	74.8	77.3
TF2	49.5	48.5	65.1	67.0	TS2	94.3	90.1	111.0	108.6
TF3	60.9	61.4	80.7	85.7	TS3	91.9	87.4	108.4	106.1
TF4	116.2	121.1	141.8	143.9	TS4	83.1	80.0	102.5	101.5
TF5	119.8	117.6	138.0	133.6	TS5	67.3	65.9	86.1	88.4
TF6	106.2	97.4	112.4	110.8	TS6	108.7	105.8	126.4	122.9
TF7	98.4	89.9	110.5	104.9	TS7	46.0	44.4	70.0	70.5
TF8	89.3	77.4	98.7	91.6	TO	64.7	62.7	84.7	84.1
Remnant fluid temperatures (C)					*External solid temperatures (C)*				
TR1	70.7	65.9	92.1	90.5	TE1	47.1	46.8	65.1	66.1
TR2	69.3	67.8	89.7	89.7	TE2	51.6	52.0	72.9	73.3
TR3	61.1	58.8	81.0	80.6	TE3	45.6	44.3	74.1	75.0
TR4	61.5	60.5	81.2	83.1					

Table 3.6: Instrumented compressor experimental values in laboratory set-up.

Tables 3.6 and 3.7 show how decreasing evaporation temperature, inlet suction line, remnant gas and solid temperatures decrease, while suction and discharge orifice temperatures increase. Discharge fluid line and outlet temperature also decrease when evaporation temperature decreases.

Compressor heat transfer losses are due to both convection and radiation effects. A comparison between the different columns of these Tables shows how the results with fan ventilation (two first columns) always present lower fluid and solid temperatures. This effect is obviously due to the higher heat transfer rate of the forced convection caused by the external fan.

Comparing experimental results with and without external fan, at -23.3^{o}C of evaporation temperature (second and third columns of Tables 5 and 6), it is possible to observe that temperatures increases without external fan as follows: the three external wall shell points, TE1-TE3, and internal shell wall temperature, TS7, increase around 37%; the fluid inlet suction muffler, TF2, increases around 25%; the fluid inside discharge line, TF5-TF8, increase between 15% and 30%; the four remnant fluid gas temperatures, TR1-TR4, increase around 27%; and oil temperature, TO, also increases around 30%.

Figs. 3.15 and 3.16 show in graph form the detailed comparative results between numerical simulation and experimental data given in Table 3.5. Figs. 3.17 and 3.18 have the same comparative results for the experimental data given in Table 3.6.

Fluid inlet compressor temperature, TF1, is a boundary condition in the simulation model. Remnant fluid temperature, TR, is obtained experimentally as mean value of the experimental data between points TR1,TR2,TR3 and TR4 which present remarkable good agreement. Differences are less than 1% in all cases except Fig. 3.17 at -10.0^{o}C and Fig. 3.18 at -23.3^{o}C where numerical results are overestimated around 2 and 3% respectively.

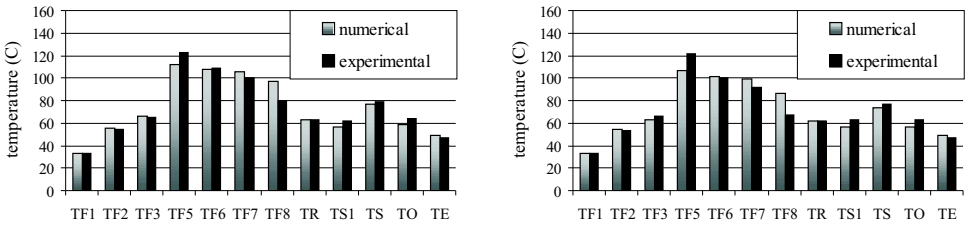

Figure 3.15: Numerical and experimental temperature values at different compressor points with fan, inside calorimeter test at -10.0^{o}C and -23.3^{o}C.

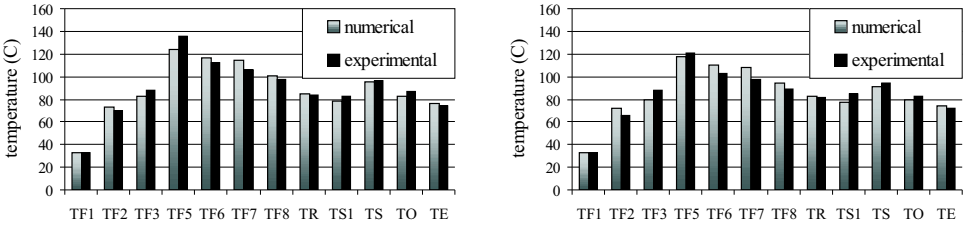

Figure 3.16: Numerical and experimental temperature values at different compressor points without fan, inside calorimeter test at -23.3^{o}C and -30.0^{o}C.

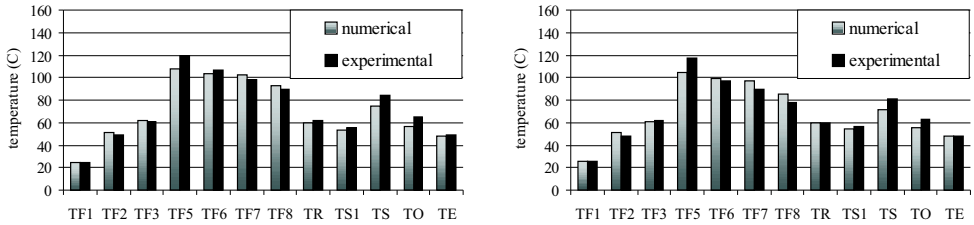

Figure 3.17: Numerical and experimental temperature values at different compressor points with fan, in laboratory test at -10.0^{o}C and -23.3^{o}C.

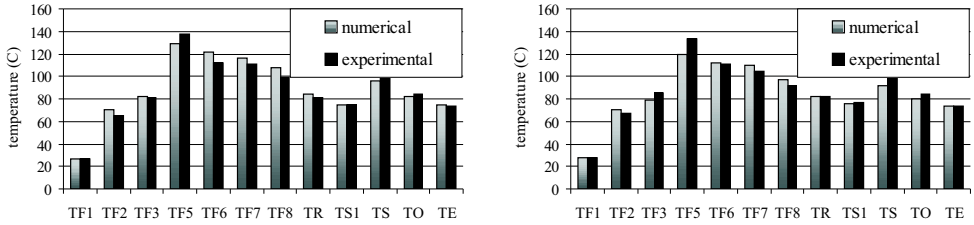

Figure 3.18: Numerical and experimental temperature values at different compressor points without fan, in laboratory test at -23.3^{o}C and -30.0^{o}C.

Fluid temperature at inlet suction muffler, TF2, is always overestimated between 2 and 8.9%, while fluid temperature at inlet suction orifice, TF3, is in general underestimated between -1% and 8.2%. That indicates remnant fluid temperature near inlet suction muffler is lower than mean remnant fluid temperature, while fluid heat transfer coefficient inside suction muffler is probably underestimated. It is interesting to remark that radiation between the electrical motor and the suction muffler is not negligible.

Cylinder head fluid temperature, TF5, shows some relevant discrepancies between numerical results and experimental data. Numerical predictions underestimate these temperatures between 2.5% and 12%. As possible reasons for these results can be the thermal conductivity influence through crankcase and cylinder head, together with probable underestimation of the heat transfer coefficient in the cylinder head.

Numerical values of the discharge fluid temperatures, TF6, TF7 and TF8, are slightly overestimated around 5%, from -2% to 9%, in all the studied cases, except outlet compressor temperature in Fig. 3.15 where higher differences are obtained. An important aspect to be considered in the discharge line is fluid pressure pulsations, which has to be introduced in the heat transfer correlations in a more accurate way.

Solid shell temperature, TE, which represents mean value between TE1, TE2 and TE3, is predicted with a slightly underestimation lower than 0.5%. Muffler temperature, TS1, is underestimated between 1% and 6%. Experimental crankcase temperature, TS, is evaluated as the mean value between the solid compression chamber temperature, TS4, and the external solid crankcase temperature, TS5. This value is also underestimated around 2% and 4%.

Oil temperature, TO, is always numerically underestimated between 4% when fan is not working, and 8% with external fan.

3.5.3 Detailed comparative results (II)

A second hermetic reciprocating compressor has been instrumented in detail with special attention on pressure volume diagram experimental data (see paragraph 3.4). A first group of detailed experimental results have been obtained for a specific case studied.

The experimental instrumentation has provide the instantaneous absolute pressure evolution along suction muffler, compression chamber and cylinder head vs. half crank angle degree. The instantaneous piston position has also been obtained. Both instantaneous compression chamber pressure and piston position allow to know experimental pV diagram.

The experimental temperature maps allow to evaluate the direct gas mass fraction from inlet compressor to suction muffler.

Both pressure distributions and pV diagrams have been numerically compared. The comparison between experimental and numerical pV diagrams with ideal pV di-

agram facilitate differences between numerical and experimental isentropic efficiency, suction and discharge energy losses.

Both numerical results and experimental data allow to compare absolute instantaneous pressure in different strategic points under periodical conditions. Fig. 3.19 shows comparative pressure maps in the three following points: outlet suction muffler, compression chamber and cylinder head.

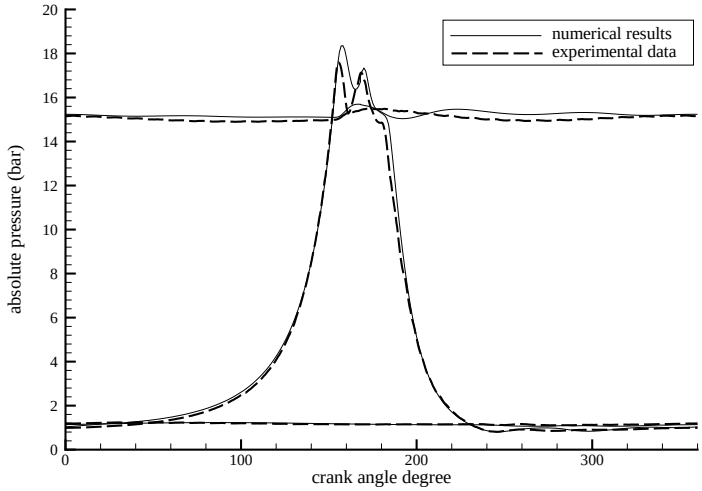

Figure 3.19: Comparative pressure results at the: suction, compression and discharge chambers.

Comparative pressure results obtained between numerical solution and experimental data show that differences are: between 1–2% on discharge pressure, with a maximum value of approximately 2.2% in crank angle positions of 190 degrees and 230 degrees; between 2–4% on suction pressure only with a maximum value of 7% around crank angle position of 260 degrees; about 8% on compression chamber pressure, except crank angle positions between 0 and 150 degrees with differences around 10%, and between 180 and 200 degrees with differences of approximately 12%.

In general, pressure comparative results show same differences as global comparative results presented in previous sections. Although, these are preliminary results for the case studied, it is interesting to remark some relevant aspects. All comparative pressure results during compression and expansion processes present a remarkable agreement. In general, there is a slight shift between numerical results and experimental data, even though both results depend on instantaneous piston position, which

is taken into account. Differences appear basically when discharge valve is opened or during suction process. These differences are essentially due to effective flow area and modal analysis of the reed valve used in the numerical model.

Fig. 3.20 shows both numerical results and experimental data on pressure volume diagram for the case studied. With these values, it is possible to compare numerical and experimental compression work, or indicated work, together with isentropic efficiency and its detachment.

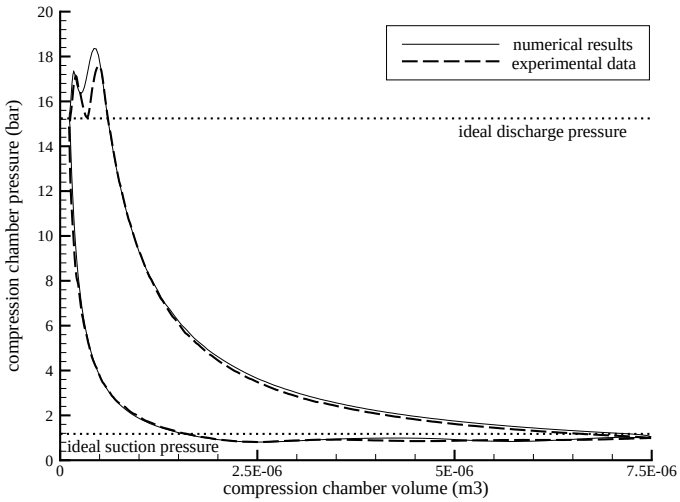

Figure 3.20: Comparative pressure volume diagram.

Table 3.7 shows compression work per mass unit, and its detachment for each one of their four work processes in the pressure volume diagram: compression, discharge, expansion and suction.

	w_{cp} [kJ/kg]	w_c [kJ/kg]	w_d [kJ/kg]	w_e [kJ/kg]	w_s [kJ/kg]
experimental	100.0	104.71	40.87	-23.24	-22.30
numerical	98.26	105.83	40.07	-23.26	-24.38

Table 3.7: Comparative results of indicated work per mass unit and its detachment.

Discrepancies between numerical results and experimental data are around 2%, except expansion work with differences lower than 0.1% and suction work with differences around 8%.

Fig. 3.20 shows that pV area corresponding to numerical results is higher than experimental one, while Table 3.8 shows numerical compression work is lower than experimental one. It should be kept in mind that first values correspond to compression power, $\dot{W}_{cp}$, while the others values correspond to compression work per mass unit w_{cp}. In this studied case, experimental mass flow rate obtained is lower than the numerical one.

Based on isentropic efficiency detachment explained in detail in next chapter 4.6, Table 3.8 shows isentropic efficiency for numerical results and experimental data, together with its different contributions: compression, discharge, expansion and suction efficiencies. Due to the lack of experimental information of opening and closing valve time, these efficiencies have been estimated considering the areas below and above the suction and discharge ideal pressures.

	η_s [%]	η_{wc} [%]	η_{wd} [%]	η_{we} [%]	η_{ws} [%]
experimental	70.9	76.1	90.5	111.6	97.4
numerical	72.2	74.9	91.0	111.8	99.4

Table 3.8: Comparative results of isentropic efficiency and its detachment.

Isentropic efficiency and all its efficiency detachment have differences lower than 2%, which really shows reasonable good agreement.

Finally, it is interesting to highlight that discharge work efficiency and suction work efficiency are approximately 90% and 98.5% for the case studied, while expansion work efficiency has a value higher than 100%.

3.6 Conclusions

An extensive experimental validation of a numerical simulation model of the thermal and fluid dynamic behaviour of hermetic reciprocating compressors has been carried out. Experimental tests have been performed in a standard calorimeter set-up and in a laboratory set-up. Different working fluids (R134a, R600a and R404A), compressors capacities (between 7.5 and 16 cm^3) and compressor ratios (evaporation temperatures from -35^{o}C to 7.2^{o}C) have been tested.

Furthermore, a first hermetic reciprocating compressor has been instrumented in detail and the experimental thermal detailed maps of temperatures in different

parts of the compressor domain has been obtained. Comparisons between numerical results and experimental data show that in general volumetric efficiency and COP are slightly underestimated for low compression ratios and slightly overestimated for high compression ratios. Thermal detailed results show the influence of the local heat transfer coefficients on both fluid and solid temperature distribution. In suction line heat transfer coefficients between fluid flow and compressor walls are slightly underestimated, while they are slightly overestimated on compression chamber. Even though reasonable good agreement has been obtained, more detailed experimental instrumentation and detailed CFD studies in some strategic compressor zones should be performed in detail.

A second hermetic reciprocating compressor has been also instrumented in detail and experimental detailed pressure maps in three strategic parts of the compressor domain has been performed. Absolute instantaneous pressures have been compared between numerical results and experimental data for the compression chamber together with suction and discharge chambers. The methodology applied allows to measure directly the pressure level for pV diagrams. Even though the agreement is remarkable, more effort should be made in improving some parts of the model. Specifically some aspects related to effective flow area estimation.

Our research group is working in this direction to get a better understanding of the complex phenomena involved and to generate more accurate empirical information to improve the capabilities of the mathematical model developed.

References

[1] F. Escanes, A. Oliva, C.D. Pérez-Segarra, and F.X. Flores. Numerical simulation of a single stage vapour compression refrigerating unit. In *International Compressor Engineering Conference*, pages 139–144, Purdue University, IN, USA, 1994.

[2] J. Rigola, F. Escanes, A. Oliva, and C.D. Pérez-Segarra. Numerical study of a single stage vapor compression refrigerant unit using non-contaminant refrigerants. In *International Compressor Engineering Conference*, pages 77–82, Purdue University, IN, USA, 1996.

[3] J. Rigola, C.D. Pérez-Segarra, O. García-Valladares, J.M. Serra, M. Escribà, and J. Pons. Numerical study and experimental validation of a complete vapour compression refrigerating cycle. In *International Compressor Engineering Conference*, pages 201–206, Purdue University, IN, USA, 1998.

[4] J. Rigola, C.D. Pérez-Segarra, O. García-Valladares, J.M. Serra, M. Escribà, and J. Pons. Analysis of hermetic reciprocating compressors- parametric study and experimental validation. In *International Conference on Compressors and Their Systems*, pages 203–212, City University, London, UK, 1999.

[5] J. Rigola, C.D. Pérez-Segarra, A. Oliva, J.M. Serra, M. Escribà, and J. Pons. Advanced numerical simulation model of hermetic reciprocating compressors. parametric study and detailed experimental validation. In *International Compressor Engineering Conference*, pages 23–30, Purdue University, IN, USA, 2000.

[6] J. Rigola, C.D. Pérez-Segarra, G. Raush, A. Oliva, M. Escribà, J. Jover, and F. Escanes. Experimental studies of hermetic reciprocating compressors with special emphasis on pv diagrams. In *International Compressor Engineering Conference*, pages C4–1, Purdue University, IN, USA, 2002.

[7] National Institute of Standards and Technology. Nist thermodynamic and transport properties of refrigerants and refrigerant mixtures - refprop version 6.01. Gaithersburg, MD, USA, 1998.

[8] W.A. Meyer. *An investigation into heat transfer processes in a small hermetic refrigeration compressor*. PhD thesis, Purdue University, Indiana, USA, 1987.

[9] A. Cavallini, L. Doretti, G.A. Longo, L. Rosseto, B. Bella, and A. Zanneiro. Thermal analysis of a hermetic reciprocating compressor. In *International Compressor Engineering Conference*, pages 535–540, Purdue University, IN, USA, 1996.

[10] Pérez-Segarra, J. C.D., Cadafalch, J. Rigola, and A. Oliva. Numerical study of turbulent fluid flow through valves. In *International Conference on Compressors and Their Systems*, pages 399–408, City University, London, UK, 1999.

[11] J. Rigola, C.D. Pérez-Segarra, A. Oliva, J.M. Serra, M. Escribà, and J. Pons. Parametric study and experimental validation of small hermetic refrigeration compressors using a complete advanced numerical simulation model. In *International Compressor Engineering Conference*, pages 737–742, Purdue University, IN, USA, 1998.

[12] R. Liu and Z. Zhou. Heat transfer between gas and cylinder wall of refrigerating reciprocating compressor. In *International Compressor Engineering Conference*, pages 110–115, Purdue University, IN, USA, 1984.

[13] F. Fagotti, M.L. Todescat, R.T.S. Ferreira, and A.T. Prata. Heat transfer modelling in a reciprocating compressor. In *International Compressor Engineering Conference*, pages 605–610, Purdue University, IN, USA, 1994.

l

Chapter 4

Thermal and fluid dynamic characterization

4.1 Introduction

A review of the different parameters which characterize the thermal and fluid dynamic behaviour of hermetic reciprocating compressors is presented. Some new parameters are introduced to get a better understanding of the complex physical processes involved in this kind of compressors. All the parameters have been tested on the basis of the numerical solutions obtained by means of numerical simulation code developed and considering a wide range of working conditions, refrigerant fluids and compressor capacities. Attention is focused on predicting the performance of hermetic reciprocating compressors under different working conditions and using the above mentioned non-dimensional parameters.

Then, the objective of this chapter is to review and present different physically meaningful parameters that characterize the reciprocating compressor behaviour, their influence detachment and evolution under different working conditions.

Different authors present several parameters to define compressor behaviour. Villadsen and Boldvig [1] base compressor efficiency on volumetric and isentropic efficiencies and COP. They study experimentally the influence on compressor ratio, speed and length of stroke for different refrigerant fluids. Scalabrin and Bianco [2] work on experimental thermodynamic analysis of the mechanical and thermal performance of compressors as function of compressor speed. They study torque, mechanical power, volumetric efficiency and COP considering a wide range of working conditions. MacGovern and Harte [3] present an overall exergy analysis for compressor performance, which take into account exergy destruction rates, using a global numerical thermodynamic model. Tassou and Quershi [4] analyze experimentally the performance of compressors for different fluids on the basis of volumetric efficiency, isentropic efficiency and COP. Stouffs et al. [5] present a detailed group of physical parameters

for compressor performance and their prediction (volumetric effectiveness, indicated efficiency, reversible heat transfer, etc.) on the basis of a global thermodynamic model considering polytropic coefficients to evaluate compression and expansion processes.

In the present study, the most important compressor parameters to define compressor performance are: volumetric efficiency, isentropic efficiency, heat transfer efficiency, and mechanical and electrical motor efficiency. Some of these parameters have been split to get a better understanding of the physical phenomena. Other parameters that help to compressor behaviour analysis are: pressure pulsation due to noise reduction and exergy analysis due to available energy improvements and the coefficient of performance COP, which characterizes compressor influence under the whole refrigerating system.

4.2 Ideal thermodynamic compressor behaviour

The majority of the non-dimensional compressor parameters which define the thermal and fluid dynamic compressor behaviour are related with different values corresponding to an hypothetic and ideal thermodynamic compressor model.

The main hypothesis of this ideal model are as follows: steady state cycle (periodical conditions), negligible kinetic and potential variations, isentropic process and ideal gas. The compressor scheme is based on three zones: one suction plenum chamber, one compression chamber and one discharge plenum chamber. Thus, inlet compressor conditions are directly inlet suction plenum conditions.

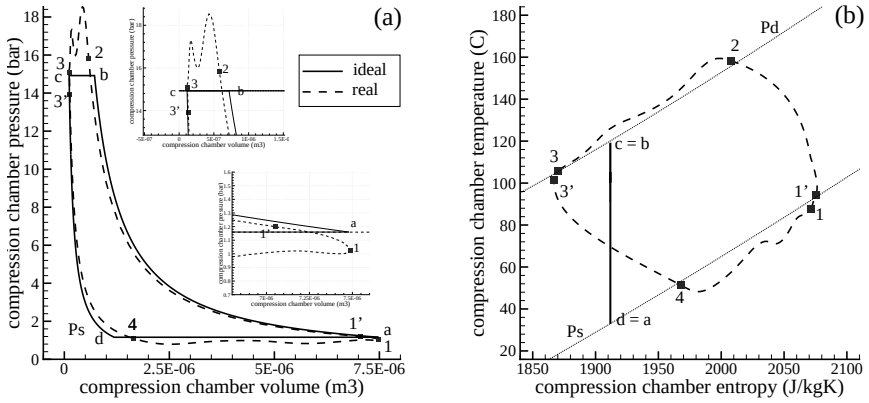

Figure 4.1: pV and Ts diagram inside compressor chamber volume (ideal and real processes).

Both pressure-volume and temperature-entropy evolution in the compression chamber are shown in Fig.4.1. The ideal thermodynamic operating cycle presents four processes: i) isentropic compression process of the gas contained in V_a at the inlet temperature and pressure conditions to outlet temperature and pressure conditions in V_b; ii) isobaric and isothermal discharge of the gas contained in V_b minus the remaining gas in V_c; iii) isentropic expansion process of the gas contained in V_c at the outlet temperature and pressure conditions to inlet temperature and pressure conditions in V_d; iv) isobaric and isothermal suction of gas from V_d to V_a.

With all these assumptions the minimum input parameters required to define the compressor behaviour are: displacement volume, dead volume, inlet gas pressure, outlet gas pressure, nominal frequency, inlet gas temperature and thermodynamic fluid properties (suction gas density and isentropic coefficient).

Based on the input data explained, and considering the hypothesis above mentioned, ideal mass flow rate, ideal outlet temperature and the ideal or isentropic compression work can be obtained as follows:

$$\dot{m}_{ideal} = \rho_{in} V_{cl} \bar{f}_n \left[1 + c\left(1 - \Pi\right)\right] \tag{4.1}$$

$$T_{out} = T_{in}\left[1 + \Pi^{(\gamma-1)/\gamma}\right] \tag{4.2}$$

$$\dot{W}_{ideal} = \rho_{in} V_{max}\left[1 - \frac{c}{1+c}\Pi^{(1/\gamma)}\right]\bar{f}_n = \frac{\dot{m}_{ideal} p_{in}}{\rho_{in}}\frac{\gamma}{\gamma-1}\left[\Pi^{(\gamma-1)/\gamma} - 1\right] \tag{4.3}$$

where Π is the compression ratio between discharge and suction pressure, and V_{max} is the maximum cylinder capacity.

The ideal or isentropic work can be split into the four parts that compose the compression cycle, ie., compression (ab), discharge (bc), expansion (cd) and suction (da) as can be seen in Fig. 4.1a. Then, $\dot{W}_{ideal} = \dot{W}_{iso} = \dot{W}_{ab} + \dot{W}_{bc} + \dot{W}_{cd} + \dot{W}_{da}$, where:

$$\dot{W}_{ab} = -\frac{p_{in} V_{max}}{1-\gamma}\left[\Pi^{(\gamma-1)/\gamma} - 1\right] \qquad \dot{W}_{bc} = -p_{in} V_{max}\left[\frac{c}{1+c}\Pi - \Pi^{(\gamma-1)/\gamma}\right] \tag{4.4}$$

$$\dot{W}_{cd} = -\frac{p_{in} V_{max}}{1-\gamma}\frac{c}{1+c}\left[\Pi^{(1/\gamma)} - \Pi\right] \qquad \dot{W}_{da} = -p_{in} V_{max}\left[1 - \frac{c}{1+c}\Pi^{(1/\gamma)}\right] \tag{4.5}$$

4.3 Compressor behaviour parameters

The reciprocating compressor behaviour can be described by means of a compressor parameter set. A selection of a minimum of non-dimensional parameters needed to describe the compressor performance has been carried out. Volumetric, isentropic, heat transfer, mechanical and electrical motor efficiencies define all thermal and fluid dynamic behaviour of compressors. COP facilitates the interaction between compressor and the rest of refrigerating equipment. The rest of the parameters, pressure pulsation and exergy balances help to improve compressor behaviour in noise reduction, maximum available efficiencies, etc.

4.3.1 Volumetric efficiency

One of the most important parameters of the global behaviour of hermetic reciprocating compressors is the volumetric efficiency, which is defined as the relation between the actual mean mass flow rate and the maximum one: $\eta_v = \dot{m}/\left(\rho_{in} V_{cl} \bar{f}_n\right)$, where ρ_{in} refers to the gas density entering into the shell.

In order to have a better understanding of this parameter, a quick look on the compression cycle shown in Fig. 4.1 is useful. Firstly, after the suction valve is closed at point 1', the piston compresses the gas inside the compression chamber until the discharge valve begins to open at point 2. The gas is discharged from point 2 to 3', where the discharge valve closes. Discharge valve closes slightly after piston reached the Top Dead Center (TDC) at point 3. Then the gas left inside the cylinder is expanded until its pressure is low enough to open the suction valve at point 4. Finally, a new fresh charge enters the compression chamber from point 4 to 1' slightly after the Bottom Dead Center (BDC) is reached of point 1. Valves are opened or closed depending on different aspects such as: gas conditions inside the compression chamber, pressures in suction and discharge manifolds (p_s and p_d respectively), pressure drop through the valves, etc.

From the definition of the volumetric efficiency, and taking into account the different processes described above, Escanes [6] proposed a decomposition of this parameter into different parts using the following equations (see Fig. 4.1a):

$$\eta_v = \frac{\dot{m}}{\rho_{in} V_{cl} \bar{f}_n} = \frac{m_{13}}{\rho_{in} V_{cl}} \frac{\bar{f}}{\bar{f}_n} \left[1 + \frac{m_{1'1} - m_{3'3}}{m_{13}}\right] \tag{4.6}$$

In this expression, the mass of the gas contained in the compressor chamber in a process from point 'i' to point 'j' is represented by m_{ij}, which is the difference of the instantaneous mass inside the cylinder at these points, i.e., $m_{ij} = m_j - m_i$. For convenience, equation 4.6 is approximately defined as:

$$\eta_v \approx \frac{m_{max}}{\rho_{in} V_{cl}} \cdot \frac{m_{13}}{m_{max}} \cdot \frac{\bar{f}}{\bar{f}_n} \cdot \left[1 + \frac{m_{1'1}}{m_{13}}\right] \cdot \left[1 - \frac{m_{3'3}}{m_{13}}\right] = \eta_{id} \cdot \eta_{irr} \cdot \eta_{\omega} \cdot \eta_{suc} \cdot \eta_{dis} \quad (4.7)$$

The first volumetric efficiency η_{id} corresponds to an ideal compression process; this efficiency only takes into account the gas expansion in the clearance volume, and can be obtained from equation (4.1). The second efficiency term, η_{irr}, takes into account the irreversibilities due to friction, heat transfer, leakages, etc. The third term, η_{ω}, is a consequence of the difference between the nominal frequency and the real one, which is basically due to mechanical and electrical motor losses. The delay in closing the suction valve, after the BDC is reached, is considered in the fourth term, η_{suc}, which is usually greater than 1 (super-charging process). The last term, η_{dis}, represents the delay in closing the discharge valve after the TDC is reached.

4.3.2 Isentropic efficiency

The second meaningful non-dimensional parameter that defines the thermodynamic behaviour of compressors is the isentropic efficiency, which is defined as the relation between the isentropic compression work, equation (4.3), and the real compression work: $\eta_s = \dot{W}_{iso}/\dot{W}_{cp}$, or in terms of the specific work, $\eta_s = w_{iso}/w_{cp}$. Both works can be split into the different compression steps (compression, discharge, expansion and suction). It is interesting to remark the differences due to real and ideal compression work at each of the four compressor processes inside compression chamber which are able to be evaluated as:

$$\eta_s = \frac{w_{iso}}{w_{cp}} = \frac{w_{ab} + w_{bc} + w_{cd} + w_{da}}{w_{1'2} + w_{23'} + w_{3'4} + w_{41'}} \quad (4.8)$$

Or using algebra:

$$\eta_s = 1 + \frac{w_{ab} - w_{1'2}}{w_{cp}} + \frac{w_{bc} - w_{23'}}{w_{cp}} + \frac{w_{cd} - w_{3'4}}{w_{cp}} + \frac{w_{da} - w_{41'}}{w_{cp}} \quad (4.9)$$

Defining the different contributions (compression, discharge, expansion and suction) to the isentropic efficiency as: $\eta_{wc} = e^{((w_{ab} - w_{1'2})/w_{cp})}$, $\eta_{wd} = e^{((w_{bc} - w_{23'})/w_{cp})}$, $\eta_{we} = e^{((w_{cd} - w_{3'4})/w_{cp})}$ and $\eta_{ws} = e^{((w_{da} - w_{41'})/w_{cp})}$, the following final expression is obtained:

$$\eta_s = 1 + ln\left(\eta_{wc} \cdot \eta_{wd} \cdot \eta_{we} \cdot \eta_{ws}\right) \quad (4.10)$$

4.3.3 Heat transfer efficiency

A non-dimensional parameter that defines the behaviour of compressors is the heat transfer efficiency, which is defined as the relation between the total energy transfer to the fluid (compression work + heat transfer gains) and the real compressor work:

$$\eta_q = \left(w_{cp} + q_{fluid}\right)/w_{cp} \tag{4.11}$$

The heat transfered gains, q_{fluid}, are defined as the heat exchanged during all compressor process, i.e. from the moment the fluid enters through the shell until the fluid goes out along the discharge tube. This heat transfer process can be detached into three compressor zones: suction line (q_{sl}), compression chamber (q_{cc}) and discharge line (q_{dl}). Evaluating heat transfer efficiency in a similar manner as the isentropic efficiency, equation (4.10), the following heat transfer efficiencies for the three zones (suction, compression and discharge) can be defined as: $\eta_{q_{sl}} = e^{(q_{sl}/w_{cp})}$; $\eta_{q_{cc}} = e^{(q_{cc}/w_{cp})}$ and $\eta_{q_{dl}} = e^{(q_{dl}/w_{cp})}$. Then heat transfer efficiency can be expressed in a similar way:

$$\eta_q = 1 + ln(\eta_{q_{sl}} \cdot \eta_{q_{cc}} \cdot \eta_{q_{dl}}) \tag{4.12}$$

4.3.4 Mechanical, electrical and heat losses efficiencies

The influence of the electrical motor, mechanical transmission and external heat losses from the shell to the environment should be considered in a specific way. Thus, mechanical efficiency (η_m) and electrical efficiency (η_e) are defined as:

$$\eta_m = w_{cp}/w_m \qquad \eta_e = w_m/w_e \tag{4.13}$$

where w_m and w_e represent mechanical and electrical works.

Based on an energy balance in all the hermetic reciprocating compressor, and over a complete cycle (under periodical conditions), the total energy transfer to the fluid is equal to the total energy transfer between compressor shell and environment (specific electrical consumption + specific heat transfer losses from the shell to the environment), $w_{cp} + q_{fluid} = w_e - q_{shell}$. Then,

$$\eta_{q_{shell}} = \frac{w_e - q_{shell}}{w_e} = \eta_q \cdot \eta_m \cdot \eta_e \tag{4.14}$$

Equation (4.14) shows a direct relationship between heat losses efficiency from shell to environment and mechanical, electrical and heat transfer efficiencies inside compressor.

4.3.5 Coefficient of Performance

Considering the whole refrigerating system, the non-dimensional parameter that defines its global thermodynamic behaviour in the whole refrigeration process is the COP (coefficient of performance), which relates evaporator refrigerating capacity with electrical power consumption, or alternatively compression work. Coefficient of performance is easily detached as a function of different efficiencies presented above:

$$COP = \frac{\dot{Q}_{ev}}{\dot{W}_e} = \frac{\Delta h_{evap}}{w_{iso}} \cdot \eta_m \cdot \eta_e \cdot \eta_s = K \cdot \eta_m \cdot \eta_e \cdot \eta_s \tag{4.15}$$

where K is the non-dimensional ratio between evaporator heat rate per mass unit and isentropic work.

4.3.6 Pressure pulsations

Instantaneous refrigerant pressure, at each time-step or crank angle degree considered, and at different compressor locations allows to have a periodical function of local pressure vs. time.

Post processing Fast Fourier Transform (FFT) analysis allows to obtain amplitude pressure maps vs. frequency. The rms pressure at each compressor point studies helps to identify critical frequencies of source of noise due to fluid pressure pulsations.

Different acoustic parameters can be defined to study critical zones, the influence on geometry, noise reduction, etc. [7].

The meaningful non-dimensional acoustic parameters considered in the present work are Sound Pressure Level and the Transmission Losses, defined for this study as follows.

$$SPL = 20log_{10}\frac{p}{p_{ref}} \qquad TL = 20log_{10}\frac{p_i}{p_t} \tag{4.16}$$

where p indicates the rms pressure at each point studied, p_{ref} is a constant pressure considered as a reference pressure, while p_i and p_t are the incident and the transmitted pressure in the selected zone to be studied. In this case, p_{ref} has been evaluated as the sound pressure on the air (20μPa).

Sound pressure level in different strategic compressor locations helps to know the maximum amplitude in the main frequencies, which is useful tool to try to reduce source of noise. Transmission losses from any inlet areas to any outlet areas gives a value of noise reductions or amplifications in mufflers, resonators, etc.

4.3.7 Exergy analysis

Together with energy and entropy thermodynamic balances, it is advisable to carry out overall exergy analysis in order to quantify irreversibilities [8]. Combining the first law of thermodynamics and the second low of thermodynamics based on entropy, the second law of thermodynamics based on exergy or available energy (maximum work that could be derived if the system were allowed to come to equilibrium with environment) can be written. Considering periodical conditions, exergy equation is as follows:

$$\dot{I} = -\left(\sum \dot{m}_o \xi_{to} - \sum \dot{m}_i \xi_{ti}\right) + \sum \int \delta Q_{fluid} \left(1 - \frac{T_o}{T_w}\right) + \dot{W}_{cp} \tag{4.17}$$

Thus, exergy destruction or irreversibilites are determinated by: convective exergy flux ($\dot{\Xi}_c = \sum \dot{m}_o \xi_{to} - \sum \dot{m}_i \xi_{ti}$), exergy associated to heat transfer gains ($\dot{\Xi}_Q = \sum \int \delta Q_{fluid} \left(1 - T_o/T_w\right)$) and exergy associated to input compressor shaft work $\dot{W}_{cp}$.

$$\dot{I} = -\dot{\Xi}_c + \dot{\Xi}_Q + \dot{W}_{cp} \tag{4.18}$$

The exergy efficiency of hermetic reciprocating compressor can be defined as the ratio between exergy flux and exergy associated to input compressor work. This ratio allows to compare the well-used available energy and the lost available energy.

$$\eta_\xi = \dot{\Xi}_c / \dot{W}_{cp} \tag{4.19}$$

4.4 Numerical results

The numerical results presented in this chapter are a characterization of the performance of an hermetic reciprocating compressor under different working conditions, by means of the non-dimensional parameters mentioned in the previous section 4.3.

All the numerical parameters have been obtained on the basis of the numerical simulation model presented in chapter 2, and after a careful verification of the quality of the numerical solution and an extensive experimental validation presented in the previous chapter 3.

The results correspond to the Unidad Hermética commercial hermetic reciprocating compressor with a 7.5 cm^3 cylinder capacity, working with R134a and a nominal frequency of 50 Hz. The following single stage vapour compression low pressure cycle has been considered: both inlet compressor temperature and outlet condenser temperature of 32^{o}C , condensation temperature of 55^{o}C and evaporation temperature of

-23.3^{o}C. Ambient temperature is fixed at 32^{o}C. Table 4.1 shows numerical illustrative results for the different evaporation temperatures considered.

T_{ev}	$\dot{m}$	w_{cp}	q_{fluid}	η_v	η_{id}	η_{iso}	η_q	η_m	η_e	COP
(^oC)	(kg/h)	(kJ/kg)	(kJ/kg)	(%)	(%)	(%)	(%)	(%)	(%)	
-10.0	7.63	74.3	-10.9	69.0	92.6	73.3	85.3	92.2	83.5	1.908
-16.5	5.28	86.1	-24.1	65.2	89.9	73.7	72.0	91.5	83.0	1.633
-23.3	3.81	96.3	-38.2	60.4	87.1	73.7	60.2	90.7	81.3	1.420
-30.0	2.36	111.2	-62.7	52.6	82.4	73.3	43.6	89.3	76.4	1.142
-35.0	1.70	121.2	-81.7	46.4	79.1	72.5	32.5	88.0	73.4	0.994

Table 4.1: Numerical results for different evaporation temperatures considered.

4.4.1 Volumetric efficiency detachment

Table 4.1 shows volumetric efficiency and ideal volumetric efficiency for the studied cases. Both group of values decrease almost linearly when evaporation temperature increases.

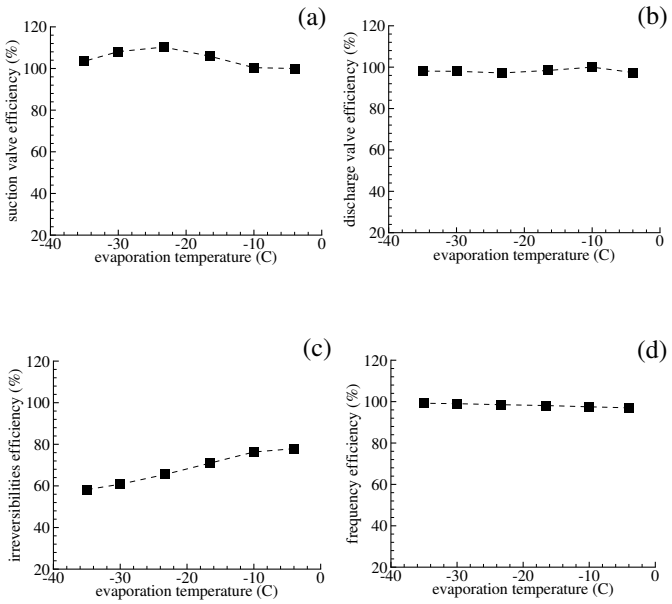

Figure 4.2: Volumetric efficiency detached. (a) η_{suc}; (b) η_{dis}; (c) η_{irr}; (d) η_{ω}.

Figs. 4.2a and 4.2b show suction and discharge valve efficiency respectively. Suction valve efficiency gives values greater than 100%, which indicates supercharging effects. Suction valve efficiency has almost a maximum -20 ^oC of evaporation temperature. Discharge valve efficiency always has an values closer under 100%. Fig. 4.2c shows irreversibilities efficiency, which increases when evaporation temperature increases. Thus, irreversibilities decreases when evaporation temperature increases. Fig. 4.2d shows that frequency efficiency is almost constant for the studied cases.

In general, most of hermetic reciprocating compressors tested follow same tendencies indicated in these figures, except suction and discharge valve efficiencies (Figs. **??**c and **??**d) which strongly depends on valve stop position, orifice diameter, valve properties (mass, stiffness, damping, etc.).

4.4.2 Isentropic efficiency detachment

Table 4.1 also shows real compression work and isentropic efficiency respectively for the studied cases, while Fig. 4.3 show isentropic efficiency ratios detached. Isentropic efficiency is almost constant with a maximum close to 73% around -23.3^{o}C of evaporation temperature.

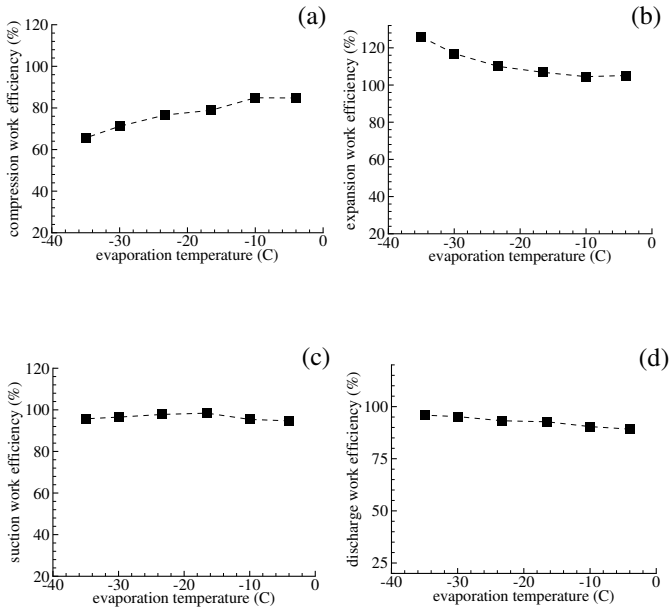

Figure 4.3: Isentropic efficiency detached. (a) η_{wc}; (b) η_{we}; (c) η_{ws}; (d) η_{wd}.

Figs. 4.3a and 4.3b show compression and expansion work efficiency respectively. Compression work efficiency increases when evaporation temperature increases tending to 80%. Expansion work efficiency decreases when evaporation temperature increases always over 100%. Figs. 4.3c and 4.3d show suction and discharge work efficiency respectively. The first one has a maximum value at approximately -20$^{\circ}C$ of evaporation temperature, while the second one decreases when evaporation temperature increases.

Compression and expansion work per mass flow unit increases when evaporation temperature increases, i.e. both work necessary to compress and work obtained in the expansion are greater when evaporation temperature increases. However, suction and discharge work per mass unit are very similar in all cases.

4.4.3 Heat transfer efficiency detachment

Fig. 4.4 shows the results of the heat transfer efficiency and its detachment for the numerical cases tested.

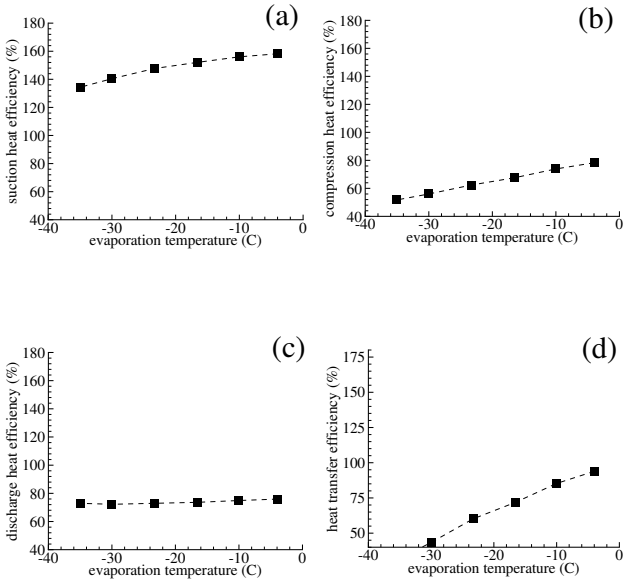

Figure 4.4: Heat transfer efficiency detached. (a) $\eta_{q_{sl}}$; (b) $\eta_{q_{cc}}$; (c) $\eta_{q_{dl}}$; (d) η_q

Fig. 4.4a shows that suction heat efficiency increases when evaporation temperature increases although tending to a value around 160%. Fig. 4.4b shows that

compression heat efficiency increases almost linearly when evaporation temperature increases always under 100%. Fig. 4.4c shows that discharge heat efficiency is almost constant, increasing slightly when evaporation temperature increases. Finally, Fig. 4.4d clearly shows that global heat transfer efficiency increases linearly when evaporation temperature increases.

4.4.4 Pressure pulsations ratios

Fig. 4.5 shows SPL values along different strategic compressor points during a periodical cycle. The results presented ranges from 0 to 4000 Hz.

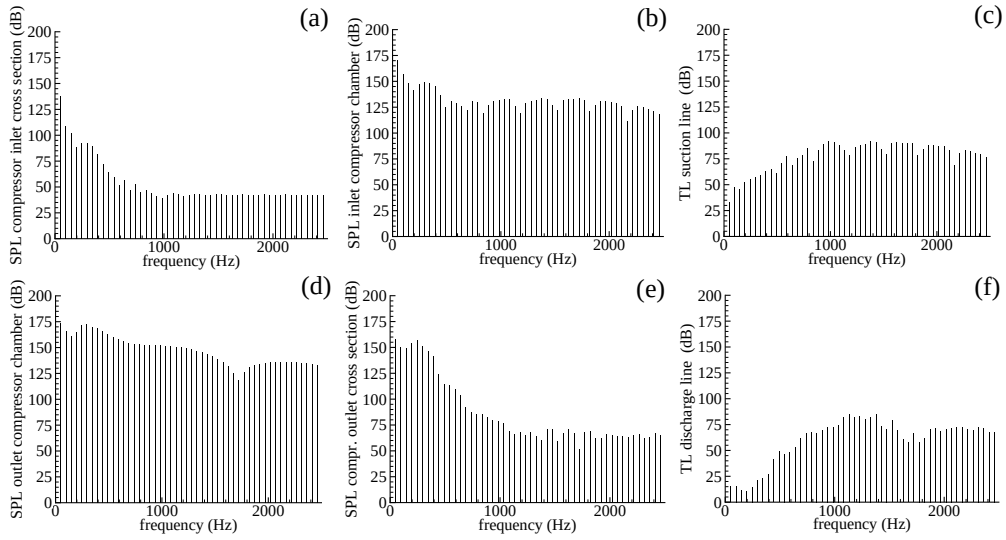

Figure 4.5: Global acoustical numerical results.

Sound Pressure Level is obtained at different compression locations: inlet compressor section Fig. 4.5a, suction compression chamber Fig. 4.5b, discharge compression chamber Fig. 4.5d and outlet compressor section Fig.4.5e. As can be seen, pressure pulsations at inlet compressor cross section decrease from 50 Hz to 2000 Hz, similar to the outlet compressor cross section, although with less amplitude.

Inlet and outlet compression chamber section present pressure pulsations along all the frequency range with amplitudes between 125 and 175 dB.

Figs. 4.5c and 4.5f present Transmission Losses due to Sound Pressure Level at suction and discharge lines respectively. Transmission Losses in the suction muffler have a similar behaviour than [9] with different minimum points from 50 Hz to 6000

Hz, and with a maximum around 2000 Hz. Transmission Losses in the discharge line have only one maximum point at 1500 Hz and then decrease when frequency increases.

4.4.5 Exergy efficiency ratio

The different contributions to the exergy balances are shown in Fig. 4.6 as function of the evaporation temperatures, or compression ratios: convective exergy flux $\dot{\Xi}_c$ (Fig. 4.6a), exergy associated to heat transfer gains $\dot{\Xi}_Q$ (Fig. 4.6b) and irreversibilities $\dot{I}$ (Fig. 4.6c). Exergy associated to compressor shaft work is equal to compression work values in Table 4.1. Exergy associated to compressor shaft work $\dot{W}_c$ and convective exergy flux $\dot{\Xi}_c$ almost increase linearly when evaporation temperature decreases. Exergy associated to heat transfer $\dot{\Xi}_Q$ is almost constant for the different compressor ratios, while irreversibilities $\dot{I}$ increase between 20W for low evaporation temperatures (-35^oC) to 50W for high evaporation temperatures (-5^oC).

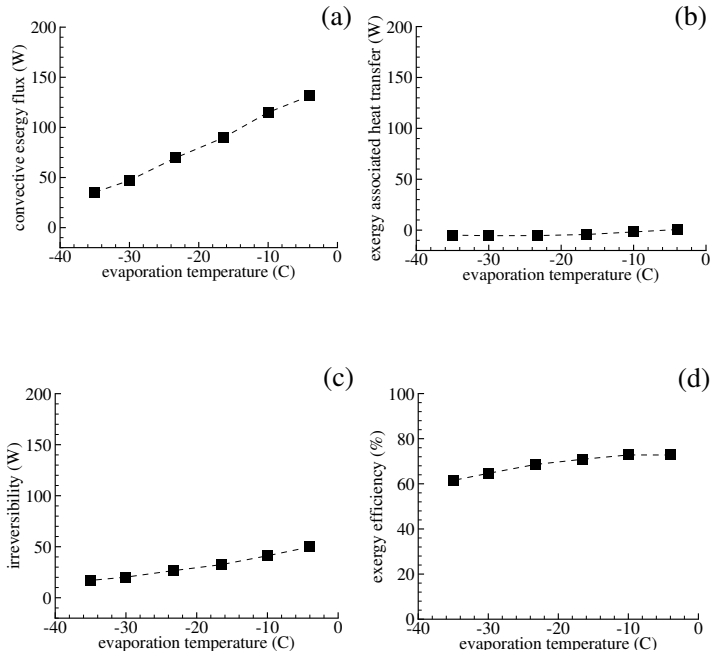

Figure 4.6: Exergy efficiency detached: (a) $\dot{\Xi}_c$; (b) $\dot{\Xi}_Q$; (c) $\dot{I}$; (d) η_ξ

Finally, Fig. 4.6d shows exergy efficiency for this kind of compressors, which is around 72% with a maximum at -20^oC of evaporation temperature.

4.5 Conclusions

A review of different hermetic reciprocating compressors parameters performances has been carried out. New parameters for compression behaviour from numerical simulation model has been also presented. The parameters section, their detachment and physical meaning have been shown.

Illustrative numerical results obtained from the advanced numerical simulation model have been used to carry out a study of the different compressor parameters performances presented in this chapter.

The results have shown the importance of these parameters in compressor behaviour. Their detachment has demonstrated how performance can be improved on the basis of these parameter studies. The detailed parametrization will also allow a more accurate development of simple models for the simulation of whole cycles.

4.6 Nomenclature

COP	Coefficient of Performance
c	clearance ratio
$\bar{f}$	mean frequency (Hz)
$\bar{f}_n$	nominal mean frequency (Hz)
$\dot{I}$	exergy destruction (W)
K	evaporator heat rate vs. isentropic work ratio per mass unit
m	mass inside compression chamber volume (kg)
$\dot{m}$	mass flow rate at given cross section (kgs^{-1})
q_{fluid}	fluid heat exchanged per mass unit (Jkg^{-1})
q_{shell}	heat transfer losses per mass unit (Jkg^{-1})
$\dot{Q}_{ev}$	refrigerating capacity (W)
p	absolute pressure (Pa)
SPL	sound pressure level
T	temperature (^oC)
T_o	dead state temperature (^oC)
T_w	wall temperature (^oC)
TL	transmission losses
V_{cl}	displacement volume (m^3)
V_{max}	total cylinder volume (m^3)
w	work per fluid mass unit (Jkg^{-1})
$\dot{W}_{cp}$	real compressor power consumption (W)
$\dot{W}_{iso}$	isentropic compressor power consumption (W)
$\dot{W}_e$	electrical power consumption (W)
*G*reek letters	
γ	isentropic coefficient (c_p/c_v)
Δh_{evap}	evaporation heat rate per mass unit (J/kg)
η	efficiency ratio *(%)*
ξ	total specific exergy (Jkg^{-1})
$\dot{\Xi}$	exergy (W)
Π	pressure ratio
ρ	density (kgm^{-3})

References

[1] V. Villadsen and F.V. Boldvig. Reciprocating compressor design for high efficiency. In *ASHRAE Transactions*, pages 819–825, 1981.

[2] G. Scalabrin and G. Bianco. Experimental thermodynamic analysis of a variable-speed open reciprocating refrigeration compressor. *International Journal of Refrigeration*, 17(1):68–75, 1994.

[3] J.A. McGovern and S. Harte. An exergy method for compressor performance analysis. *International Journal of Refrigeration*, 18(6):421–433, 1995.

[4] S.A. Tassou and T.Q. Qureshi. Comparative performance evaluation of positive displacement compressors in variable speed refrigeration applications. *International Journal of Refrigeration*, 21(1):29–41, 1998.

[5] M. Stouffs, P.and Tazerout and P. Wauters. Thermodynamic analysis of reciprocating compressors. *International Journal of Thermal Science*, 40:52–66, 2001.

[6] F. Escanes. *Numerical simulation of the thermal behaviour of diferent components of compression refrigerating system. Experimental validation. Application to non-contaminant rerigerants.* PhD thesis, Technical University of Catalonia, UPC, CTTC, UPC, Terrassa, Barcelona, 1995.

[7] W. Soedel. *Mechanics, Simulation and Design of Compressor Valves, Gas Passages and Pulsation Mufflers.* Purdue University Short Courses, IN, USA, 1992.

[8] A. Bejan. *Advanced Engineering Thermodynamics.* John Wiley & Sons, NY, 1988.

[9] B. Alfano, E. Biscaldi, and F. Rozza. Suction muffler optimization in a reciprocating compressor. In *International Compressor Engineering Conference*, pages 747–752, Purdue University, IN, USA, 1994.

Chapter 5

Parametric studies

5.1 Introduction

This chapter is focused on presenting different parametric studies of commercial hermetic reciprocating compressors. Special attention has been focused on geometrical aspects (suction and discharge valve orifice diameters and valve stop positions, muffler geometries, valve plates, etc.) together with electrical motor influence and working conditions (different fluid refrigerants, low and high evaporation temperatures, etc.).

The influence of these different aspects over some of the non-dimensional parameters presented in the previous chapter: volumetric efficiency, η_v, power consumption, coefficient of performance COP, etc. for different working conditions is going to be presented.

The idea of this chapter is to show the possibilities offered by the simulation model and its final objective, a better understanding of the thermal and fluid dynamic behaviour of hermetic reciprocating compressors to improve the design of these equipments.

5.2 Orifice diameter influence

Different parametric studies have been carried out in order to show the influence of suction and discharge valve diameter. Different cases are presented for different fluids, geometries and working conditions. Numerical simulation results show the tendencies of two non-dimensional parameters (ηv and COP) and the optimal values for the cases and conditions studied.

5.2.1 Suction valve diameter influence

A whole of numerical simulation results has been obtained changing suction valve orifice diameter from 8.5 mm to 10.5 mm for a hermetic reciprocating compressor of

16.0 cm^3 working with R600a. Originally, the suction valve diameter was 9.5 mm. Table 5.1 shows numerical results at four different evaporation temperature conditions -10.0^{o}C, -23.3^{o}C, -30^{o}C and -35^{o}C respectively, maintaining condenser temperature at 55^{o}C.

	η_v(%)				COP			
T_{ev} (^oC)	-10.0	-23.3	-30.0	-35.0	-10.0	-23.3	-30.0	-35.0
$d_{suc} = 8.5mm$	73.8	65.9	57.7	50.2	1.973	1.489	1.229	1.042
$d_{suc} = 9.5mm$	75.1	66.1	58.4	51.0	1.995	1.504	1.241	1.052
$d_{suc} = 10.5mm$	75.4	66.6	59.4	52.6	2.008	1.516	1.250	1.059

Table 5.1: Influence of suction valve diameter at different evaporation temperatures (R600a, V$_d$= 16 cm^3, T$_{con}$ = 55^{o}C).

Results presented in Table 5.1 show how volumetric efficiency increases between 2% and 4% with evaporation temperatures between -10.0^{o}C, -35^{o}C respectively, when the suction orifice diameter increases. In the same cases, COP increases when the suction orifice increases between 1.6% at higher evaporation temperatures and around 1.8% at lower evaporation temperatures. Minimum differences in volumetric efficiency and COP are at -23.3^{o}C of evaporation temperature. Numerical results present a better behaviour on volumetric efficiency, and COP with values closer to 10.5 mm instead of 8.5 mm, although this improvement is limited by physical space in valve plate. Together with these conclusions, other aspects have to be considered in the design of the orifice itself (eg. round inlet orifice, etc.).

5.2.2 Discharge valve diameter influence

A numerical simulation has been carried out changing discharge valve orifice diameter from 6.5 mm to 8.0 mm for a hermetic reciprocating compressor of 12.0 cm^3 working with R404A. Originally, the discharge valve diameter was around 6.5 mm. Table 5.2 shows numerical results at three different evaporation temperature conditions -10.0^{o}C, -23.3^{o}C and -35^{o}C respectively, maintaining condenser temperature at 55^{o}C. The same Table presents clearance ratio ϵ for the different diameters evaluated. Fig. 5.2.2 shows the same results of volumetric efficiency and COP on graph.

In general, volumetric efficiency decreases when the discharge orifice diameter increases between 2%, 3% and 5% for evaporation temperatures between -10.0^{o}C to and -35.0^{o}C respectively. Volumetric efficiency presents an evolution strongly affected by clearance ratio. However, COP increases when the discharge orifice increases between 1.5% at higher evaporation temperatures, around 0.5% with an evaporation temperature of -23.3^{o}C and almost with no variations at lower evaporation temperatures.

Consequently, the optimum discharge valve diameters is a compromise between good volumetric efficiency and adequate COP, although results presented show points near optimum solution for cases studied.

	$d_{disch}(mm)$	6.5	6.8	7.2	8.0
	$\epsilon(\%)$	1.70	1.75	1.81	1.98
T_{ev} = -10.0^{o}C	$\eta_v(\%)$	68.5	68.1	67.9	67.1
	COP	1.847	1.853	1.862	1.877
T_{ev} = -23.3^{o}C	$\eta_v(\%)$	63.1	62.8	62.3	61.4
	COP	1.369	1.372	1.374	1.376
T_{ev} = -35.0^{o}C	$\eta_v(\%)$	55.7	55.2	54.8	53.0
	COP	0.999	0.999	1.000	0.997

Table 5.2: Influence of discharge valve diameter at different evaporation temperatures (R404A, V_d= 12 cm^3, T_{con} = 55^{o}C).

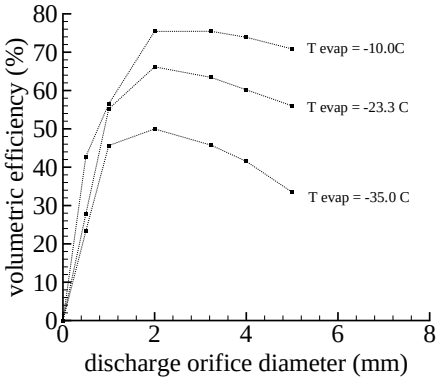

Figure 5.1: Volumetric efficiency vs. discharge orifice valve diameter.

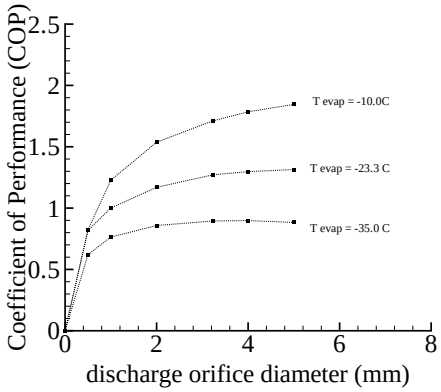

Figure 5.2: COP vs. discharge orifice valve diameter.

5.3 Valve stop influence

The influence of suction and discharge valve stop have also been studied in a similar way than orifice diameters. Different cases are presented for different fluids, geometries and working conditions. Suction valve stop influence is studied taking

into account a wide range of lengths including the possibility to not have valve stop. Discharge valve stop is studied in a small range of values, looking for the optimum value for the case studied.

5.3.1 Suction valve stop influence

Table 5.3 presents several numerical results changing suction valve stop from 1.27 mm to non-valve stop for a hermetic reciprocating compressor of 16.0 cm^3 working with R600a. Originally, suction valve stop was 1.5 mm.

Table 5.3 shows numerical results at same conditions of Table 5.1, and presents clearance ratio ϵ for the different valve stop evaluated.

	$z_{max}(mm)$	1.27	1.50	3.00	–
	$\epsilon(\%)$	1.159	1.174	1.273	1.075
T_{ev} = -10.0^{o}C	$\eta_v(\%)$	75.0	75.1	75.1	72.1
	COP	1.980	1.995	2.015	2.003
T_{ev} = -23.3^{o}C	$\eta_v(\%)$	66.8	66.1	62.3	64.3
	COP	1.498	1.504	1.498	1.505
T_{ev} = -30.0^{o}C	$\eta_v(\%)$	58.8	58.4	54.4	60.1
	COP	1.237	1.241	1.231	1.248
T_{ev} = -35.0^{o}C	$\eta_v(\%)$	50.2	51.0	51.3	55.6
	COP	1.047	1.052	1.057	1.062

Table 5.3: Influence of suction valve stop at different evaporation temperatures (R600a, V_d= 16 cm^3, T_{con} = 55^{o}C).

Results presented show different tendencies depending on compression ratio studied. When valve stop increases between 1.27 and 3.0 mm, volumetric efficiency is constant at -10.0^{o}C of evaporation temperature, decreases around 6% at -23.3^{o}C and at -30.0^{o}C of evaporation temperature and increases around 2% at -35.0^{o}C. When there is non valve stop, volumetric efficiency decreases around 4% at -10.0^{o}C of evaporation temperature and increases for the rest of studied cases. Thus, volumetric efficiency presents an evolution depending on clearance ratio values. COP presents same tendency in all considered cases and increases around 1% when suction valve stop increases.

Consequently, these cases depend not only on the suction valve stop considered, but also on compression ratio desired, which strongly influences the valve dynamics.

5.3.2 Discharge valve stop influence

Table 5.4 presents several numerical results changing discharge valve stop from 0.4 mm to 1.0 mm for a hermetic reciprocating compressor of 9.0 cm^3 working with R134a. Originally, suction valve stop was 0.45 mm.

	$\eta_v(\%)$			COP		
$T_{ev}(^oC)$	-10.0	-23.3	-35.0	-10.0	-23.3	-35.0
$z_{max} = 0.40mm$	74.34	62.26	44.79	1.665	1.247	0.886
$z_{max} = 0.45mm$	74.57	62.53	44.94	1.698	1.262	0.890
$z_{max} = 0.60mm$	75.01	63.11	45.39	1.768	1.292	0.899
$z_{max} = 0.80mm$	75.16	63.27	45.34	1.820	1.311	0.904
$z_{max} = 1.00mm$	75.17	63.04	45.24	1.848	1.319	0.905

Table 5.4: Influence of discharge valve stop at different evaporation temperatures (R134a, V$_d$= 9 cm^3, T$_{con}$ = 55^{o}C).

Results presented show that in all cases volumetric efficiency increases around 1% when discharge valve stop increases from 0.4 mm to 1.0 mm Improvements considering COP are much better, i.e., COP increases when discharge valve stop increases between 10%, 5% and 2% for evaporation temperatures between -10.0^{o}C, -23.3^{o}C and -35.0^{o}C respectively.

Consequently, higher discharge valve stop clearly improves volumetric efficiency and COP, although this improvement could be limited by noise production, which is an essential aspect of a compressor design.

5.4 Geometrical suction mufflers influence

Numerical simulation are presented considering four different suction mufflers configurations for a hermetic reciprocating compressor of 14.0 cm^3 and 16.0 cm^3 working with R600a.

Fig. 5.3 shows the different configurations considered. M1 configuration supposes two suction muffler in series; M2 considers one large tube with two resonators; M3 presents one tube with resonator adding a second chamber, and M4 shows one chamber adding to a tube with resonator.

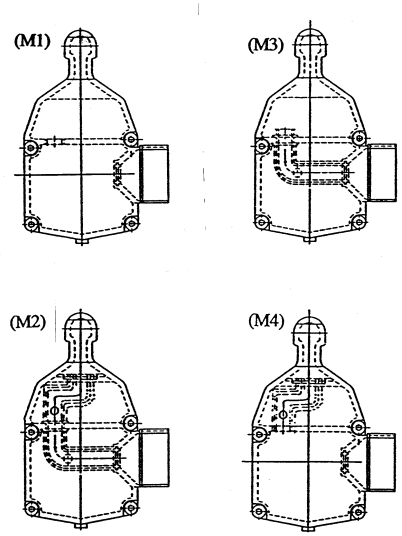

Figure 5.3: Different suction mufflers configurations

Tables 5.3 and 5.4 show volumetric efficiency and COP numerical results for 14.0cm^3 and 16.0cm^3 respectively, considering four different evaporation temperature conditions -10.0^{o}C, -23.3^{o}C, -30^{o}C and -35^{o}C and maintaining condenser temperature at 55^{o}C.

	M1		M2		M3		M4	
T_{ev}	η_v	COP	η_v	COP	η_v	COP	η_v	COP
(^{o}C)	*(%)*	*(-)*	*(%)*	*(-)*	*(%)*	*(-)*	*(%)*	*(-)*
-10.0	76.4	1.901	76.6	1.897	76.4	1.881	76.2	1.888
-23.3	69.2	1.483	69.6	1.469	68.8	1.460	68.3	1.463
-30.0	61.3	1.239	61.3	1.223	60.7	1.215	60.1	1.216
-35.0	52.6	1.065	51.8	1.045	51.8	1.042	51.1	1.042

Table 5.5: Influence of suction muffler configuration at different evaporation temperatures (R600a, V$_d$= 14 cm^3, T$_{con}$ = 55^{o}C).

	M1		M2		M3		M4	
T_{ev}	η_v	COP	η_v	COP	η_v	COP	η_v	COP
(^oC)	(%)	(-)	(%)	(-)	(%)	(-)	(%)	(-)
−10.0	74.5	2.012	75.8	2.022	75.1	1.996	74.9	2.010
−23.3	66.0	1.528	66.5	1.519	65.7	1.504	65.1	1.509
−30.0	59.0	1.267	58.3	1.250	58.4	1.243	57.6	1.244
−35.0	51.7	1.077	50.0	1.055	50.8	1.052	49.8	1.050

Table 5.6: Influence of suction muffler configuration at different evaporation temperatures (R600a, V_d= 16 cm^3, T_{con} = 55^{o}C).

Both Tables show volumetric efficiency has a maximum for M2 configuration between -10^{o}C and -23.3^{o}C evaporation temperatures, while is has a maximum for M1 configuration between -30^{o}C and -35^{o}C evaporation temperatures. Minimum volumetric efficiency is presented for M4 configuration in all cases with differences between 2% compared with M2, and between 3% compared with M1.

Together with volumetric efficiency, COP has maximum value for M1 configuration in all cases. Minimum COP is presented for M3 configuration in all studied cases.

Table 5.5 shows differences in COP between 0.7% and 2% from higher evaporation temperatures to lower evaporation temperatures, while Table 5.6 shows differences in COP between 0.1% and 2.5% from higher evaporation temperatures to lower evaporation temperatures. Even though the suction mufflers with two chambers in series, M1, present better COP and volumetric efficiency in all cases studied, this solution is not the optimum due to noise production.

5.5 Valve plate and electrical motor torque influence

Several cases have been tested considering different valve plates and motors. The following cases are some illustrative results of this type of comparisons for different suction (S1 and S2) and discharge (D1 and D2) valve geometries, presented in Fig. 5.4. Table 5.7 shows different main natural frequencies for valves mentioned above. S1 and D1 have more stiffness than S2 and D2.

Results of different cases are presented in Table 5.8 for a hermetic reciprocating compressor of 14 cm^3 working with R600a, for different compression ratios maintaining condenser temperature equal to 55^{o}C, where case A considers a valve plate with S1 as suction valve with an orifice of 8.3 mm and D1 as discharge valve with an orifice

of 6.3 mm; case B considers a valve plate with S2 as suction valve with an orifice of 9.5 mm, and D2 as discharge valve with an orifice of 7.3 mm. Finally, case C is equal to case A increasing motor capacity around 20%.

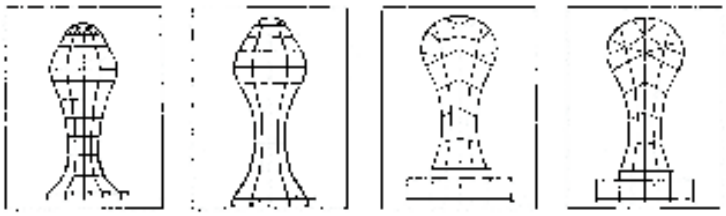

Figure 5.4: Different suction valve geometries; left: A1 and A2 and discharge valve geometries; right: D1 and D2.

natural frequencies	*S1 valve*	*S2 valve*	*D1 valve*	*D2 valve*
1^{st} *frequency (Hz)*	175.40	151.19	377.48	308.44
2^{nd} *frequency (Hz)*	1185.58	997.05	2198.37	1783.62
3^{rd} *frequency (Hz)*	1325.04	1144.90	2855.68	2407.78

Table 5.7: Suction and discharge valves main natural frequencies (S: suction; D: discharge).

	case A		*case B*		*case C*	
T_{ev}	η_v	COP	η_v	COP	η_v	COP
(^oC)	(%)	(-)	(%)	(-)	(%)	(-)
−10.0	76.4	1.881	76.1	1.936	76.3	1.975
−23.3	68.8	1.460	68.7	1.495	68.3	1.507
−30.0	60.7	1.215	60.7	1.240	60.4	1.256
−35.0	51.8	1.042	53.1	1.062	53.1	1.078

Table 5.8: Influence of different valve plates and motor at different evaporation temperatures (R134a, V_d= 14 cm^3, $T_{con} = 55^oC$).

Comparison between case A and B shows volumetric efficiency almost presents no differences; while COP increases between 0.5% and 3% from -30.0^{o}C to -10.0^{o}C of evaporation temperatures, respectively.

Comparison between case A and C shows volumetric efficiency increases slightly around 0.5% and COP increases between 3% and 5% from -30.0^{o}C to -10.0^{o}C of evaporation temperatures. Then, both cases almost present no changes in volumetric efficiency, although they present higher COP values when evaporation temperature increases.

5.6 Compressor working conditions

All cases presented above have been carried out for different compression capacities, different fluid refrigerants and working conditions even though all boundary evaporator and condenser temperatures have been considered equal to low pressure single stage vapour compression cycles and nominal frequency equal to 50Hz. Following subsections show different illustrative results working at high evaporation pressure, at lower evaporation pressures and working at different frequencies. Different valve displacements, pV diagrams, instantaneous frequency and motor torque, together with instantaneous heat transfer and work inside compression chamber are going to be some of the detailed comparative results presented.

5.6.1 Compressor at high evaporation temperatures

Table 5.9 presents several numerical results for a hermetic reciprocating compressor of 16.0 cm^3 working with R134a; considering different relative high evaporation temperatures from -10.0^{o}C to 15.0^{o}C, and also at different condenser temperatures from 45.0^{o}C to 55.0^{o}C.

	T_{con}					
	45.0^{o}C		55.0^{o}C		65.0^{o}C	
T_{ev}	η_v	COP	η_v	COP	η_v	COP
($^o C$)	(%)	(−)	(%)	(−)	(%)	(−)
-10.0	74.3	1.563	71.1	1.385	67.7	1.231
0.0	77.9	2.000	75.2	1.766	72.1	1.554
7.2	79.5	2.326	77.1	2.036	74.1	1.769
15.0	79.9	2.699	77.6	2.329	74.7	1.970

Table 5.9: Influence of different high evaporation temperatures at different condenser conditions at different evaporation temperatures (R134a, V$_d$= 16 cm^3).

Table 5.9 shows how increasing evaporation temperature and maintaining condensation temperature the volumetric efficiency and COP increase. Differences in vol-

umetric efficiency are higher between -10.0^{o}C and 0.0^{o}C evaporation temperatures, than between 0.0^{o}C and 15.0^{o}C evaporation temperatures. Volumetric efficiency tends to give a maximum value. COP has the same rise for the studied ranges.

Therefore, its slope is maintained almost linear. Same Table shows how increasing condensation temperature and maintaining evaporation temperature volumetric efficiency and COP decreases. Differences in both volumetric efficiency and COP are higher at low evaporation temperatures than at high evaporation temperatures, although these differences are more obvious during COP evolution.

5.6.2 Compressor at low evaporation temperatures

Table 5.10 presents several numerical results for a hermetic reciprocating compressor of 16.0 cm^3 working with R134a; considering different lower evaporation temperatures from -10.0^{o}C to -40.0^{o}C. Fig. 5.5 presents detailed numerical results of the same cases studied.

T_{ev}	$\dot{m}$	η_v	ω	$\dot{Q}_{ev}$	$\dot{W}_E$	COP
(^{o}C)	(kg/h)	(%)	(rpm)	(W)	(W)	(-)
−10.0	15.82	65.5	2820	862.0	549.1	1.45
−30.0	5.45	54.9	2920	282.1	302.5	0.93
−40.0	2.45	41.0	2958	127.2	187.8	0.68

Table 5.10: Influence of different low evaporation temperatures at different evaporation temperatures (R134a, V$_d$= 16 cm^3, T$_{con}$ = 55^{o}C).

Fig. 5.5a shows how pV area is reduced when evaporation temperature decreases, although maximum pressure point is maintained in all cases due to discharge valve stop. Fig. 5.5b shows how discharge valve displacement has a delay to open when evaporation temperature decreases, although closing point is maintained. Suction valve at -10.0^{o}C of evaporation temperature stays always at the top of valve stop, while at -23.3^{o}C and -35.0^{o}C evaporation temperatures, suction valve has two oscillations. Suction valve has a delay to open and to close, which increases when evaporation temperature decreases. Fig. 5.5c shows how instantaneous frequency variations increases when evaporation temperature decreases, while mean frequency values decreases when evaporation temperature decreases. Instantaneous motor torque of Fig. 5.5d has maximum value at the same point of minimum instantaneous frequency value of Fig. 5.5c. Figs. 5.5e and 5.5f show instantaneous compression chamber heat transfer and work respectively. Both graphs present same delays from -35.0^{o}C to -10.0^{o}C evaporation temperatures. Compression work area decreases when evaporation temperature also decreases, while slopes are maintained equal.

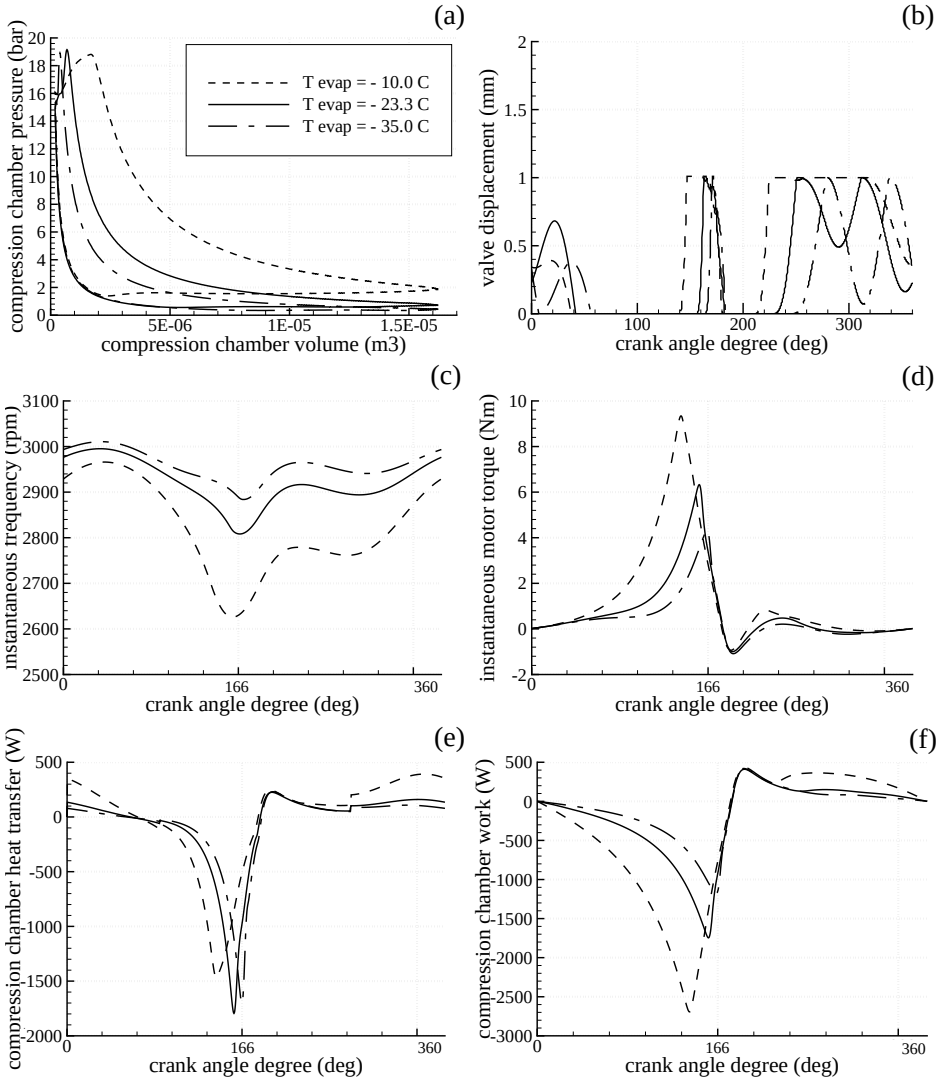

Figure 5.5: Detailed instantaneous numerical illustrative results at different low evaporation temperatures.

5.6.3 Compressor at different working frequencies

Table 5.11 presents several numerical results for a hermetic reciprocating compressor of 16.0 cm^3 working with R600a; considering different relative low evaporation temperatures -10.0^{o}C, -23.3^{o}C and -35.0^{o}C maintaining condenser temperature equal to 55.0^{o}C. The objective is to know the behaviour of this compressor reducing working frequency for all these cases.

						T_{ev}
	-10.0^{o}C		-23.3^{o}C		-35.0^{o}C	
ω	$\dot{m}$	COP	$\dot{m}$	COP	$\dot{m}$	COP
(Hz)	(kg/h)	$(-)$	(kg/h)	$(-)$	(kg/h)	$(-)$
48.3	5.51	2.052	2.77	1.493	1.18	1.065
44.0	5.04	2.085	2.41	1.499	1.09	1.074
40.0	4.63	2.121	2.27	1.527	0.99	1.050
35.0	3.99	2.147	1.96	1.540	0.91	1.090

Table 5.11: Influence of real working frequency (R600a, V_d= 16 cm^3, T_{con} = 55^{o}C).

Frequency reduction shows that, in all cases, mass flow rate is reduced around 30%, 28% and 23% at evaporation temperatures of -10.0^{o}C, -23.3^{o}C and -35.0^{o}C respectively; while COP increases around 4.5%, 3% and 2.3% at evaporation temperatures of -10.0^{o}C, -23.3^{o}C and -35.0^{o}C respectively.

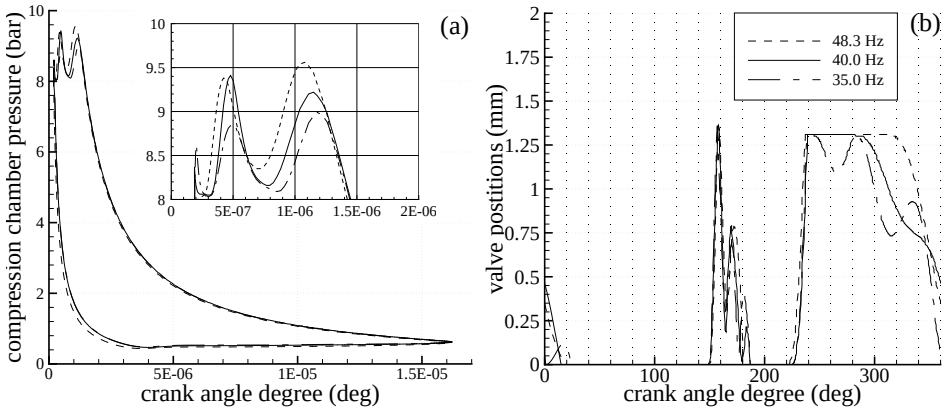

Figure 5.6: pV diagram and valve displacement working at different conditions.

Fig. 5.6a presents very similar pV diagram between different studied cases, although maximum compression chamber pressure during discharge process, decreases when working frequency decreases. Fig. 5.6b shows how suction valve working at 48.3Hz and 44.0Hz is always maintained at suction valve stop with a delay on second case; while the same valve working at 40.0Hz and 35.0Hz has several oscillations at suction valve stop. Back flow at discharge valve is present and increases when frequency is reduced. However, at -35.0^{o}C back flow is also present although decreases when frequency is reduced.

5.7 Conclusions

A parametric study of hermetic reciprocating compressors behaviour has been presented based on the numerical simulation developed. Results presented of volumetric efficiency and COP show how discharge valve diameter and suction valve stop depends on geometry (specially clearance ratio) and compression ratio (because its influence on valve dynamics) and it is observed that optimum values are a compromise between good volumetric efficiency and adequate COP. Higher values of the suction valve diameter and discharge valve give thermal improvements in all cases studied. The same conclusion is observed for lower valve stiffness. Suction muffler geometries studied present better performance without resonators and with two chambers in series. Some of the above mentioned aspects can be limited because of physical space or noise production. Finally, evolution of volumetric efficiency and COP at different evaporation temperatures, and working compressor frequencies have been numerically tested. Also, their influence on valve dynamics has been highlighted.

Chapter 6

Conclusions

6.1 Concluding remarks

The numerical simulation model presented is based on the integration of the fluid conservation equations (continuity, momentum and energy) in the whole compressor domain (compression chamber, valves, manifolds, mufflers, connecting tubes, parallel paths, etc.) using instantaneous local mean values for the different variables. It is interesting to remark how momentum equation has been taken into account in all compressor parts and the possibility of solving complex geometries (parallel paths, resonators, etc.) [1], [2] and [3].

Effective flow areas are evaluated considering multidimensional models based on modal analysis of fluid interaction in the valve. Then, second and third order natural vibration modes of valve are also considered. Better semi-analytical model on valve dynamic interaction with the fluid flow and CFD studies are able to be implemented in order to improve valve dynamic model [4].

The force balances in the crankshaft connecting rod mechanical system are simultaneously solved at each time-step. It allows to evaluate the instantaneous compression chamber volume and the different forces in the crankshaft connecting rod mechanical system. Mechanical system forces allows to know important information to predict possible over-stresses in piston, piston pin, crankshaft, connecting rod, etc. However, the resolution of flow leakage between piston and cylinder will help to improve the model and to obtain more accuracy results.

The thermal analysis of the solid elements is based on global energy balances at each macro volume considered (shell, muffler, tubes, cylinder head, crankcase, motor, etc.). Some improvements can be implemented (shell conduction, heat transfer coefficient evaluation, etc.).

The resulting governing equations (fluid flow, valve dynamics, conduction heat transfer in solids, etc.) are discretized by means of a fully implicit control volume formulation. The complete set of algebraic equations are coupled using the segregated

pressure based algorithm Semi-Implicit Method for Pressure-Linked Equations (SIMPLEC) extended to compressible flow. Second and third order schemes have been implemented for the transient terms.

Numerical results have been carefuly check to assure the quality of the solutions, i.e., verification of convergence and discretization errors in a well written code (no programming errors).

An extensive hermetic reciprocating compressor experimental validation has been presented and the experimental know-how acquired has been highlighted [2], [5] and [6]. Furthermore, two commercial hermetic reciprocating compressor have been instrumented in detail to obtain the thermal temperatures map and the pressure fluid evolutions along compressor for different working conditions. It is interesting to remark, as a novelty, the use of very small absolute pressure transducers, instead of the standard relative transducers. They allow to know instantaneous absolute pressure inside compressor chamber, without the necessity of measurement an absolute pressure outside the compression chamber (as usual in previous experimental works presented by other authors) [7], [5] and [8].

After verification process to assure the quality of the numerical solution, the mathematical model developed has been validated against the experimental data obtained in the way indicated above.

Verification and validation are esential steps in the development of a tool to assist in the design and optimization of these compressors. However, the hughe information generated for the code has been parametrized in a such a way that global behaviour is characterized by a few parameters.

Standard parameters (volumetric efficiency, isentropic efficiency, COP, etc.) have been used together with new detailed parameters specially developed: volumetric efficiency detachment, isentropic efficiency detachment, zonal heat transfer efficiency [9].

Finally, a parametric study of hermetic reciprocating compressors behaviour has been carried out [10], [11]. Results presented show the influence of different aspects (geometry, valves, motor, working conditions, etc.) in the compressor behaviour. Interesting results shows how volumetric efficiency and COP on discharge valve diameter and suction valve stop depend on geometry (specially clearance ratio) and compression ratio (because its influence on valve dynamics). Also, it is observed that optimum values are a compromise between good volumetric efficiency and adequate COP. Higher values of the suction valve and discharge valve diameters give thermal improvements in all cases studied, while the same conclusion is observed for lower valve stiffness. Suction muffler geometries studied present better performance without resonators and with two chambers in series. However, some of the above mentioned aspects can be limited because of physical space or noise production. Evolution of volumetric efficiency and COP at different evaporation temperatures, and

working compressor frequencies have been numerically tested. Also, their influence on valve dynamics has been highlighted.

The parametric studies and compressor characterization detachement allows a better implementation of simplest models of the compressors in the thermal and fluid dynamic numerical simulation of vapour compressor cycles [12], [13] together with the rest of elements [14].

6.2 Future actions

The future actions can be summarized in the following four main lines:

i) improvements in the mathematical model: more accurate empirical inputs obtained from experiments and/or CFD simulations; more advanced effective flow and force area models; inclusion of flow leakage through piston and cylinder; multidimensional heat conduction in the shell; electrical motor simulation; modeling of accoustical phenomena; etc.

ii) numerical aspects: greater feasibility for analyzing more complex flow configurations; more efficient solvers; coupled methods for continuity and momentum equations; etc.

iii) experimental infrastructure: experimental evaluation of valve position; experimental infrastructure to obtain effective flow and force are values; experimental evaluation of compressor accoustic noise; etc.

iv) optimization of hermetic reciprocating compressors using CO_2.

References

[1] F. Escanes, C.D. Pérez-Segarra, J. Rigola, J.M. Serra, J. Pons, M. Escribà, and M. Jornet. Numerical simulation of reciprocating compressors. recent improvements and experimental validation. In *International Compressor Engineering Conference*, pages 193–198, Purdue University, IN, USA, 1996.

[2] J. Rigola, C.D. Pérez-Segarra, A. Oliva, J.M. Serra, M. Escribà, and J. Pons. Parametric study and experimental validation of small hermetic refrigeration compressors using a complete advanced numerical simulation model. In *International Compressor Engineering Conference*, pages 737–742, Purdue University, IN, USA, 1998.

[3] C.D. Pérez-Segarra, J. Rigola, and A. Oliva. Detailed numerical simulation of hermetic reciprocating compressors. part 1 : Numerical model. *International Journal of Heat Ventilation Air Conditioning and Refrigeration Research*, page accepted to be published, 2002.

[4] Pérez-Segarra, J. C.D., Cadafalch, J. Rigola, and A. Oliva. Numerical study of turbulent fluid flow through valves. In *International Conference on Compressors and Their Systems*, pages 399–408, City University, London, UK, 1999.

[5] J. Rigola, C.D. Pérez-Segarra, A. Oliva, J.M. Serra, M. Escribà, and J. Pons. Advanced numerical simulation model of hermetic reciprocating compressors. parametric study and detailed experimental validation. In *International Compressor Engineering Conference*, pages 23–30, Purdue University, IN, USA, 2000.

[6] J. Rigola, C.D. Pérez-Segarra, and A. Oliva. Detailed numerical simulation of hermetic reciprocating compressors. part 2 : Experimental validation. *International Journal of Heat Ventilation Air Conditioning and Refrigeration Research*, 2002. accepted to be published.

[7] J. Rigola, C.D. Pérez-Segarra, O. García-Valladares, J.M. Serra, M. Escribà, and J. Pons. Analysis of hermetic reciprocating compressors- parametric study and experimental validation. In *International Conference on Compressors and Their Systems*, pages 203–212, City University, London, UK, 1999.

[8] J. Rigola, C.D. Pérez-Segarra, G. Raush, A. Oliva, M. Escribà, J. Jover, and F. Escanes. Experimental studies of hermetic reciprocating compressors with special emphasis on pv diagrams. In *International Compressor Engineering Conference*, pages C4–1, Purdue University, IN, USA, 2002.

[9] C.D. Pérez-Segarra, J. Rigola, and A. Oliva. Thermal and fluid dynamic characterization of hermetic reciprocating compressors. In *International Compressor Engineering Conference*, pages C4–2, Purdue University, IN, USA, 2002.

[10] J. Rigola, C.D. Pérez-Segarra, and A. Oliva. Parametric study of hermetic reciprocating compressors. In *International Compressor Engineering Conference*, pages 529–534, Purdue University, IN, USA, 1996.

[11] J. Rigola, C.D. Pérez-Segarra, A. Oliva, J.M. Serra, M. Escribà, and J. Pons. Parametric study of hermetic reciprocating compressors. detailed numerical analysis and experimental validation. In *International Conference on Compressors and Their Systems*, pages 189–198, City University, London, UK, 2001.

[12] J. Rigola, F. Escanes, A. Oliva, and C.D. Pérez-Segarra. Numerical study of a single stage vapor compression refrigerant unit using non-contaminant refrigerants. In *International Compressor Engineering Conference*, pages 77–82, Purdue University, IN, USA, 1996.

[13] J. Rigola, C.D. Pérez-Segarra, O. García-Valladares, J.M. Serra, M. Escribà, and J. Pons. Numerical study and experimental validation of a complete vapour compression refrigerating cycle. In *International Compressor Engineering Conference*, pages 201–206, Purdue University, IN, USA, 1998.

[14] O. García-Valladares, , C.D. Pérez-Segarra, J. Rigola, and A. Oliva. Detailed numerical simulation of condensers and evaporators using pure and refrigerant mixtures. In *International Compressor Engineering Conference*, pages 201–206, Purdue University, IN, USA, 1998.